TURUN YLIOPISTON JULKAISUJA
ANNALES UNIVERSITATIS TURKUENSIS

SARJA - SER. A I OSA - TOM. 481

ASTRONOMICA - CHEMICA - PHYSICA - MATHEMATICA

DETECTION OF ILLICIT DRUGS AND DRUG PRECURSORS WITH CANTILEVER-ENHANCED PHOTOACOUSTIC SPECTROSCOPY

by

Jaakko Lehtinen

TURUN YLIOPISTO
UNIVERSITY OF TURKU
Turku 2013

From

Department of Physics and Astronomy
University of Turku
Finland

Supervised by

Tom Kuusela
Docent
Department of Physics and Astronomy
University of Turku
Finland

Reviewed by

Lauri Halonen
Professor
Department of Chemistry
University of Helsinki
Finland

Juha Toivonen
Docent
Department of Physics
Tampere University of Technology
Finland

Opponent

Markus Sigrist
Professor
Institute for Quantum Electronics
Swiss Federal Institute of Technology Zurich
Switzerland

ISBN 978-951-29-5630-2 (PRINT)
ISBN 978-951-29-5631-9 (PDF)
ISSN 0082-7002
Painosalama Oy - Turku, Finland 2013

Acknowledgements

The work presented here has been carried out in the Laboratory of Optics and Spectroscopy in the Department of Physics and Astronomy, University of Turku, during the years 2011 to 2013.

I would like to express my gratitude to my supervisor Tom Kuusela. Over the past three years, there has never been a moment when he would not have time to discuss some new results or a problem in the measurements. I am also grateful to Tom for having faith in me as a PhD student and sourcing the funding for my studies for most of the last three years.

I would to thank the guys at Gasera for their remarkably positive attitude towards my research. All the people there have been very helpful since the first time I visited. They allowed me use their instruments and sometimes even re-scheduled their own work so that I could conduct mine as planned. I would also like to thank the University of Oulu and VTT Oulu for their collaboration.

I wish to thank Dr. Kathryn S. Kalasinsky for kindly providing me with the patient hair samples for this study. Meeting her on the first day of my first scientific conference was the luckiest thing to happen and provided me direction of this study. I am also grateful to Mr. Christian Hirschmann and Dr. Juho Uotila for co-authoring.

Finally, I would like to thank Suvi for her support during this study. Especially finalizing the thesis was a bumpy ride. Thank you for not staying out of my way.

Contents

Abstract

In this study, cantilever-enhanced photoacoustic spectroscopy (CEPAS) was applied in different drug detection schemes. The study was divided into two different applications: trace detection of vaporized drugs and drug precursors in the gas-phase, and detection of cocaine abuse in hair. The main focus, however, was the study of hair samples. In the gas-phase, methyl benzoate, a hydrolysis product of cocaine hydrochloride, and benzyl methyl ketone (BMK), a precursor of amphetamine and methamphetamine were investigated. In the solid-phase, hair samples from cocaine overdose patients were measured and compared to a drug-free reference group. As hair consists mostly of long fibrous proteins generally called keratin, proteins from fingernails and saliva were also studied for comparison.

Different measurement setups were applied in this study. Gas measurements were carried out using quantum cascade lasers (QLC) as a source in the photoacoustic detection. Also, an external cavity (EC) design was used for a broader tuning range. Detection limits of 3.4 particles per billion (ppb) for methyl benzoate and 26 ppb for BMK in 0.9 s were achieved with the EC-QCL PAS setup. The achieved detection limits are sufficient for realistic drug detection applications.

The measurements from drug overdose patients were carried out using Fourier transform infrared (FTIR) PAS. The drug-containing hair samples and drug-free samples were both measured with the FTIR-PAS setup, and the measured spectra were analyzed statistically with principal component analysis (PCA). The two groups were separated by their spectra with PCA and proper spectral pre-processing. To improve the method, EC-QCL measurements of the hair samples, and studies using photoacoustic microsampling techniques, were performed. High quality, high-resolution spectra with a broad tuning range were recorded from a single hair fiber. This broad tuning range of an EC-QCL has not previously been used in the photoacoustic spectroscopy of solids. However, no drug detection studies were performed with the EC-QCL solid-phase setup.

List of publications

This thesis consists of an introductory part, followed by six research publications.

I *Drug precursor vapor phase sensing by cantilever enhanced photoacoustic spectroscopy and quantum cascade laser*
J. Uotila, J. Lehtinen, T. Kuusela, S. Sinisalo, G. Maisons, F. Terzi, I. Tittonen
in Proc. of SPIE **8545**, 85450I-1–85450I-13, 2012.

II *Sub-ppb detection of formaldehyde with cantilever enhanced photoacoustic spectroscopy using quantum cascade laser source*
C.B. Hirschmann, J. Lehtinen, J. Uotila, S. Ojala and R.L. Keiski
Applied Physics B **111**, 603–610, 2013.

III *Spectroscopic Studies of Human Hair, Nail, and Saliva Samples Using a Cantilever-Based Photoacoustic Detection*
J. Lehtinen
International Journal of Thermophysics **34**, 1559–1568, 2013.

IV *Human Hair in the Identification of Cocaine Abuse with Cantilever-Enhanced Photoacoustic Spectroscopy and Principal Component Analysis*
J. Lehtinen, C.B. Hirschmann, R.L. Keiski and T. Kuusela
Applied Spectroscopy **67**, 846–850, 2013.

V *Cantilever Enhanced Photoacoustic Spectroscopy of Hair Microsamples*
J. Lehtinen and T. Kuusela
in Proc. of IRS^2, 130–134, 2013. DOI 10.5162/irs2013/iP10.

VI *Broadly tunable quantum cascade laser in cantilever-enhanced photoacoustic infrared spectroscopy of solids*
J. Lehtinen and T. Kuusela
Applied Physics B, 2013, paper in press, published online, DOI: 10.1007/s00340-013-5617-9.

Chapter 1

Introduction

At present, rapid detection of different molecules in small concentrations is a common requirement in applications in various fields. In fact there are multiple applications, for example in industry, atmospheric and waste monitoring, medical use, drug detection, human health, and personal safety [1–6]. As always, more sensitive techniques are constantly needed. Small concentrations of different compounds have to be detected in different phases and in different sample matrices. This implies that the measurement conditions will vary. In all cases, the target molecules are present as traces in particular matrices, for example indoor air, tissue or blood. Also, the available sample amount may be low. Another requirement that is raised in the majority of these practical applications is that the equipment should be a hand-held size or at least portable.

To be able to detect trace-level concentrations, a high sensitivity instrument is clearly needed. Sensitivity, however, is not the only sufficient condition. The method also has to be capable of distinguishing the target molecule from the possible interferents. High sensitivity to one compound is worthless if there is major cross-interference from other components that are present during the measurement. Furthermore, in many of the abovementioned applications, harmful or toxic substances are monitored, which imposes further requirements on the instruments used. These instruments have to be reliable and the measurements need to be highly repeatable. Moreover, false positive or negative results should be eliminated, or at least minimized. In short, the technique has to be sensitive, selective, reliable, fast and compact.

This study focuses on the applications in drug detection. The concerns of drug use include drug-related diseases and deaths, driving under the influence of drugs, and drug-related crime [7]. Different techniques

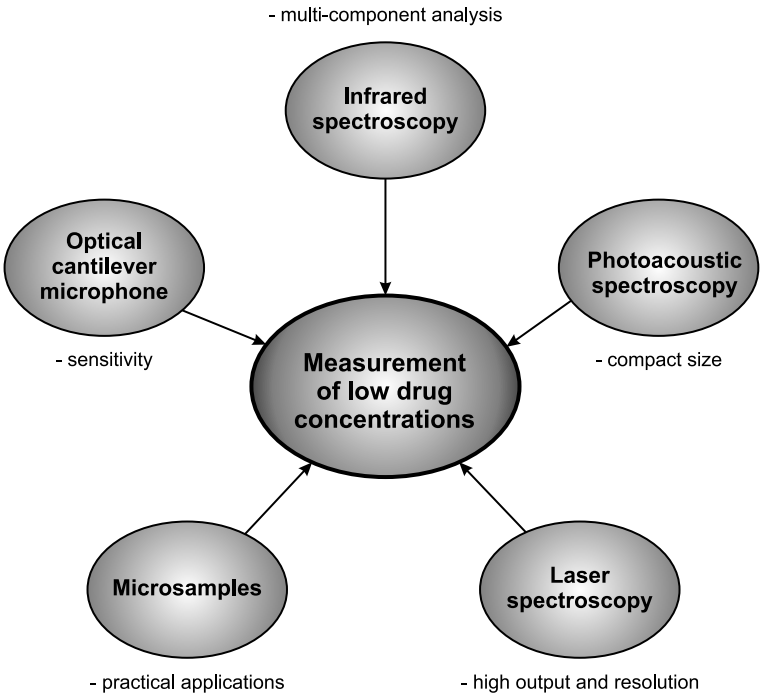

Figure 1.1: The techniques involved in the approach to the problem.

were combined in the approach to the problem, to obtain the optimal result. First, mid-infrared (IR) spectroscopy was chosen to be the core of the study for several reasons. IR spectroscopy enables the investigation of gas-, liquid-, and solid-phase samples; small concentrations of molecules in gases or liquids can be measured as well as physically small solid samples or small features on samples. Moreover, there is a possibility to meet the hand-held size requirement. At present, there are already hand-held sized commercial Fourier transform infrared (FTIR) devices. However, the sensitivity of such instruments is not sufficient for this study. Hand-held operation was also a criterion when selecting photoacoustic detection. In conventional transmission spectroscopy, long absorption paths are required in order to measure small concentrations. This is not the case with photoacoustic spectrosopy (PAS); in fact in some cases, the sensitivity of the instrument can be enhanced by decreasing the size of the photoacoustic cell and therefore the optical path. Other benefits of the photoacoustic method are that there is no need for sample processing and depth profiling capabilities in the solid-phase [8, 9]. Photoacoustic detection itself does not guarantee high sensitivity. A cantilever microphone with an op-

tical readout was thus introduced for ultimate sensitivity; several orders of magnitude higher sensitivity can be reached by the use of this optical microphone [10–12]. Further, compared to the conventional condenser microphones, the cantilever has a linear operation with a high dynamic range. Microsampling techniques in the solid-phase PAS were introduced to enable an increased signal from physically small sample sizes. Enabling truly small samples brings this technique out of laboratory research and into practical applications. Also, the photoacoustic cell design can further improve the detection of extremely small samples. Clearly, the sensitivity of the operation can be enhanced by increasing the optical power of the IR source. This leads to the use of tunable laser spectroscopy. Quantum cascade lasers (QCL) and optical parametric oscillators (OPO) can achieve tuning ranges sufficient for spectroscopy in the mid-IR range [13]. Extremely broad tuning ranges can now be achieved with the use of external cavity (EC) QCLs [14]. EC-QCL operation combines the high resolution and optical power of lasers with an increased tuning range. By combining the above-mentioned techniques it is possible to perform spectroscopy of small concentrations in small sample volumes with high resolution and a sufficient tuning range.

In this study, two different approaches–trace gas and hair analysis–, were applied in the detection of illegal substances. The main emphasis was in the study of hair samples. Trace-gas analysis can be applied in drug and drug precursor detection in several different stages. Drug precursors can be detected during transportation, for example in customs, even before the actual drug has been manufactured. Similarly, drugs can be detected in their transportation and distribution phases. Drugs and drug precursors can also be detected in the manufacturing stage, for instance during a search of a suspected clandestine laboratory. In practice, this is done by "smelling" the environment or a specific cargo. Extremely sensitive detection is needed, because the vapors extracted from solid matter are measured in a relatively large space.

Hair analysis was applied to a drug-testing scenario. Drug tests are needed, for example, in employment, general workplace testing, and for acquiring driving licenses; these tests would be more common if a simple, non-invasive and cheap method for the simultaneous detection of multiple drugs existed. Hair has been investigated here for its non-invasive measurement and long detection window. Normally, drug tests are performed by taking a blood or urine sample. Different sample matrices such as skin, fingernails, saliva and blood can also be applied to drug detection or medical purposes using PAS. In this study, the method is applied in drug detec-

tion, but it is suitable for a variety of applications in gas-, liquid-, and solid-phases.

The thesis is structured as follows: In Chapter 2, there is a short review of infrared drug detection techniques, and the photoacoustic effect and the different components used in the experimental part of the thesis are introduced. In short, these include a photoacoustic detector, optical cantilever microphone and different readout constructions, FTIR spectrometers, and laser sources. In Chapter 3, various configurations of cantilever-enhanced photoacoustic spectroscopy (CEPAS) are examined for gas- and solid-phase samples. Human hair is discussed as a sample matrix and single-fiber studies are also performed using the microsampling techniques of PAS. Drug detection studies with CEPAS are discussed in Chapter 4. First, detection of drugs and drug precursors in the gas-phase with laser photoacoustic spectroscopy (LPAS) is discussed. Methyl benzoate, a hydrolysis product of cocaine hydrochloride, and benzyl methyl ketone (BMK), a precursor of amphetamine and methamphetamine were investigated. Later, FTIR-PAS was applied in the detection of cocaine traces in human hair. Both rapid-scan and step-scan are considered. The final chapter summarizes the results of the thesis and provides some future interests for the subject.

Chapter 2

Measurement techniques

2.1 Background

Detection of drugs of abuse connects multiple areas of science, different techniques, and several ways to detect drugs. Drug detection in the gas-phase practically means measuring trace levels of vaporized chemicals in air, and thereby finding evidence of illegal substances. In this case, the evidence is found as certain spectral peaks in the mid-IR spectrum. Vapor-phase IR spectroscopy can be applied to the identification of solid compounds that have a sufficient vapor pressure at room temperature.

Vapor-phase drug detection has a wide variety of applications. These include, for example, screening individuals, buildings, vehicles, cargo, and hand-carried items and other belongings. The individuals may be arrested persons, prisoners or large numbers of people randomized from the general public. Buildings, rooms, cars or boats may be inspected if suspected of storing of drugs; in addition, vehicles and cargo may be inspected in border crossings. Hand-carried items can include handbags, luggage, packages and other mail [15].

Vapor-phase IR spectroscopy has previously been applied to illicit drug detection for hallucinogens [16], ephedrine [17], amphetamine [18], and drug precursors [18]. The vapor concentrations of different drugs can vary from particles per million (ppm) to particles per trillion (ppt) levels [15]. Therefore, extremely sensitive detection is needed. IR spectroscopy has not been the most popular choice for vapor-phase drug detection. Mainly, devices based on ion mobility spectrometry (IMS), field ion spectrometry (FIS), mass spectrometry (MS) and Raman spectroscopy have been used for this task [15]. This is due to the insufficient detection limits of the former IR spectrometers, for example hand-held FTIR spectrometers. Vapor detec-

tion can also be performed by gas cromatography/infrared spectrometry (GC/IR). GC/IR is mostly used in the separation of the individual components from drug mixtures instead of identifying drugs in the air. However, it has not found many applications in forensic use [19]. GC/IR is also generally too bulky for field use. There is a need for better and more accurate gas-phase detection techniques, and thus there are two ongoing European Commission funded projects, namely CUSTOM and DOGGIES, at the present time [20, 21]. These projects focus on the detection of drugs, drug precursors, hidden persons and explosives. Both projects utilize photoacoustic IR spectroscopy. In CUSTOM and DOGGIES, ultraviolet induced fluorescence and IMS, respectively, are also applied in parallel to IR spectroscopy.

In solid-phase detection, IR spectroscopy can be applied for two main purposes in the analysis of illicit drugs: identification, for example of street samples, and detection of drug traces [16, 22]. An evident application connected to drug-trace detection is drug testing. Drug testing can be conducted by using different sample matrices; for example, urine, blood and hair samples have all been successfully used in drug testing. Of course, urine or blood tests are the conventional method of drug testing. Cocaine has been previously studied using IR spectroscopy for its strong carbonyl group (C=O) absorption. Attenuated total reflectance (ATR) spectroscopy has been applied to cocaine detection in saliva. A detection limit of 0.020 mg/ml for cocaine in saliva was reached without any separation or extraction procedures with ATR spectroscopy [2]. The method was further enhanced by the inclusion of the one-step extraction method [23, 24]. With the extraction, a detection limit of 1 µg/ml was achieved [23]. Cocaine detection in IR spectroscopy has also been recently performed by using microfluidic techniques and QCLs [25, 26]. Hair has been studied using IR spectroscopy in the pioneering work of Kathryn S. Kalasinsky et al. [27, 28].

2.1.1 Detection of drugs in hair

Drug analysis in hair started in 1979, when opiates were successfully detected in hair [29]. Hair analysis for drugs of abuse has also been used in the detection of cocaine, marijuana, nicotine, opiates and amphetamines [30–32]. Hair samples show potential advantages over the normally used urine or blood samples; perhaps the most important advantage is the larger detection window of the drugs. The detection window in hair can be from

months to even years, compared to a couple of days in urine and blood, with most drugs [4, 31]. This larger detection window also enables the investigation of a person's drug history. As hair is essentially dead tissue, the conditions are stable and the record of the substances used could be near permanent [27]; however, given the normal hygiene practices this is not realistic [31]. Hair sampling can also be considered non-invasive, and hair samples can easily be collected and stored. Hair samples are already routinely analyzed, for example in forensic cases, occupational health and clinical toxicology [31]. The guidelines for analyzing hair for drugs are maintained by the Society of Hair Testing (SoHT) [33].

However, there are of course also drawbacks in using hair samples. These drawbacks include the drug incorporation of hair, dose-concentration relationship, bias between different samples and external contaminations [31, 32]. Drugs incorporate into hair via blood circulation, sweat and sebum, and by passive exposure [4, 32]. However, these incorporation procedures are not entirely clarified [34]. Many factors affect this incorporation, and thus the overall concentration of the drug in the hair. As the procedures are not completely known, it complicates the estimation of the original drug intake. Furthermore, there is a bias in drug incorporation between different hair types, which should be taken into account to ensure fair and standardized drug testing. Another key question is how to discriminate external contaminations, for example from environmental exposure, from actual drug abuse. Decontamination procedures are used to remove the traces of passive exposure. However, these decontamination procedures are not perfect. To acknowledge this problem, cut-off concentrations are applied in the analysis [33].

Generally, GC/MS can be considered the golden technique of drug testing in hair and is used as a standard in many of the toxicological laboratories [31–33, 35]. However, due to the sophisticated washing, separation and extraction phases in the analysis, the technique cannot be transferred directly into field use. It is advised that two techniques should be combined for a reliable result of drug usage. The techniques are usually labeled as a screening test and a confirmative test. Normally, immunoassay techniques are used in the screening and GC/MS is used for the confirmation of the drugs in the hair. The use of two orthogonal techniques also applies to drug testing in general.

In IR spectroscopy, ATR has been used for drug detection in hair. Kalasinsky et al. have successfully detected cocaine, 6-acetylmorphine and hydromorphone in hair [27, 28]. The drug levels of 150 ng/mg for cocaine,

68.8 ng/mg for 6-acetylmorphine, and 12.7 ng/mg for hydromorphone in hair were measured separately with GC/MS. The lowest detection limits were not estimated in these studies. The drug distribution in hair was detected as concentrating mainly in the medulla, which is the innermost region of hair [28]. The ATR measurement was complicated by its sample preparation procedures, and this method has not expanded as a regular hair analysis tool in drug testing. The sampling requires paraffin molding of the hair fibers and microtome operation is needed for the desired sampling depth. In addition, the single fibers have to be in good contact with the ATR crystal for a successful measurement. For small fibers, this can be a challenging task.

2.2 Photoacoustic effect

The photoacoustic effect was discovered by Alexander Graham Bell as early as 1880 [36]. Photoacoustic detection is based on the conversion of optical energy into thermal energy [9]. The principle of the photoacoustic effect is rather simple [8, 11, 37, 38]: modulated light is guided into a photoacoustic cell and absorbed by the sample gas. As a consequence, a fraction of the ground state molecular population will excite to higher energy levels. These excited states will eventually relax through radiative and non-radiative transitions. The non-radiative part heats the sample gas, which induces a thermal expansion. This thermal expansion occurs periodically due to the modulation. Because the photoacoustic cell is an enclosed space, the periodical thermal expansion generates a pressure wave. The pressure waves can subsequently be detected with a pressure sensor, in this case a microphone. In short, light is guided into the sample, but it is the acoustic waves coming out that are measured.

If compared to the photoacoustic effect of gases, the phenomenon in solids includes an extra step. The extra step relates to the solid/gas interface. The theory of the photoacoustic effect in solids was introduced in the mid-1970s by Allan Rosencwaig and Allen Gersho (RG-theory) [39], and further extended by several authors later in the 1970s [40, 41]. As a result of the absorption of photons by the sample, the thermal waves propagate to the sample surface and into the surrounding gas. According to the RG-theory, a thin layer of gas surrounding the sample surface can be considered to be working as an acoustic piston [39]. Nitrogen, or another gas that is not active in the IR region, can be used as a carrier in the photoacoustic cell. However, helium is usually preferred, due to its higher

thermal conductivity, which increases the acoustic signal. There is also back reflection by the sample surface, which notably attenuates the intensity of the photoacoustic effect [42]. The photoacoustic signal generation in the liquid-phase is similar to the solid-phase. Photoacoustic detection can also be applied on liquid samples, but the measurement is usually troublesome as the moisture content attaches into the cell windows, deteriorating their performance. In the worst case, the cell windows may become completely unusable and have to be replaced. Cell designs have been proposed especially for liquids, but as yet no commercial products are available [43].

The conventional photoacoustic detection requires three basic elements: the source, the photoacoustic cell and the pressure sensor. The source can be, for example, a blackbody radiator or a laser. The photoacoustic cell is designed to couple the acoustic excitations most efficiently and can be used in a resonant or non-resonant mode. Finally, the acoustic waves are recorded with a microphone. The most common microphone designs include a conventional condenser type microphone, a quartz resonator or an optical cantilever.

2.2.1 Photoacoustic spectroscopy in the gas-phase

Photoacoustic IR spectroscopy began in the late 1970s although single wavelength studies already existed [8]. At that time, multiple wavelength experiments were carried out using broadband sources and wavelength filters in order to measure the desired wavelengths. The filtering could be done by actual interference filters or by rotating a grating in a monochromator. The introduction of FTIR instruments was revolutionary, enabling the rapid simultaneous collection of all wavelengths. However, in PAS, the conventional condenser microphones normally lack the sensitivity that is needed in FTIR applications [11]. The use of the cantilever revolutionized the FTIR-PAS due to its higher sensitivity, enabling new applications that were previously inconvenient or out of reach [10, 11, 44, 45]. The newest revolution in photoacoustic spectroscopy of gases is the use of widely tunable lasers [46, 47]. The current development of QCLs and OPOs enables the building of spectrometers based on the photoacoustic principle that are small in size, high in spectral radiance and that have a wavelength range which is also sufficient for spectroscopy with solid samples.

Photoacoustic detection is mainly used for trace gas detection in IR spectroscopy [11, 46, 47]. Single wavelength studies are relevant in the gas-phase, because of the sharp peaks of small gas molecules, especially

at low pressures. Conversely, photoacoustic detectors are seldom used in gas-phase FTIR applications. As a result of the sharp peaks, the method is highly selective, and a single spectral line can already provide reliable information about the concentration of a particular gas in the cell. In contrast to conventional transmission spectroscopy, where the absorption length of the cell determines the detection limit, photoacoustic cells can be constructed in a small size and still have very high sensitivity [11]. The equation for the detection limit (limit of detection, LOD) for a gas-phase photoacoustic measurement is

$$LOD = \frac{c \cdot S}{3 \cdot \sigma_{RMS}}, \tag{2.1}$$

where c is the concentration of the sample gas, S is the photoacoustic signal of the sample gas, and σ_{RMS} is the root mean square (RMS) noise of the background gas, usually nitrogen. The contribution of the nitrogen background has to be subtracted from the original spectrum of sample gas in order to obtain S. PAS is a so-called zero background technique, and the spectra are generally normalized only with respect to the source output. This type of normalization is called source compensation.

2.2.2 Photoacoustic spectroscopy in the solid-phase

There are some advantages of PAS over the conventional transmission-based techniques for solid samples [8]:

- No sample preparation is necessary.
- The measurement is non-destructive.
- The technique is suitable for opaque materials.
- Depth profiling can be performed for heterogeneous or layered samples.

In many cases, these attributes are beneficial or critical for a successful measurement. A non-invasive measurement performed from the sample surface is one of the criteria in myriad applications. Due to its nature of measuring acoustic waves instead of transmitted or scattered photons, PAS is often described as an "unconventional" IR technique [8]. In the solid-phase the spectral lines are generally broad due to larger molecules, which practically prevents the applicability of the single wavelength studies.

Because photoacoustic detection is a zero-background technique, an empty sample cannot be used in the normalization of the spectra as in conventional transmission spectroscopy. Moreover, in an FTIR measurement, the optical power for different wavelengths cannot be measured directly, which is done in a laser measurement. Instead, a carbon black sample is usually applied in the normalization of the spectra. The idea is to record the spectrum of an all-absorbing sample, from which the response of the used instrument can be derived. The different variations of the reference material are, for example, carbon powder, carbon filled rubber and soot from incomplete combustion. Different materials have been suggested to be optimal, and some claim that no form of carbon can be used in normalization, and that source compensation should be used instead [48, 49]. However, different IR detectors also have different responses, and therefore affect the normalization. The normalization and the possible reference materials for PAS have been widely studied [48–52]. A reference material with high absorption, flat response and minimal characteristic IR bands is needed for performing quantitative spectroscopy. Further, usually some data processing has to be applied [8, 53]. Qualitative spectroscopy can be performed to some level, as long as the reference is the same for every sample.

Solid samples that consist of a combination of complex molecules generally have some absorption in the whole range of the spectrum and therefore the signal intensity also has to be normalized for a reasonable comparison of different spectra. The spectra are usually normalized to a certain peak or to the area of the spectrum. There are a few factors that affect the photoacoustic spectrum of a solid sample. These include the sample and sample cell size [54], sample position [52, 55] and the interstitial gas expansion of loosely packed samples, for example some powders [56]. Sample size affects the size of the photoacoustic cell, which alters the response of the cell. Usually, this effect is minor and can be ignored. However, in the case of very small samples, this effect has a significant contribution, and the sample should be normalized with a similar sized reference [54]. Further, the sample should not be elevated too near to the cell window to prevent any heat loss to the window.

Depth profiling

In IR spectroscopy, depth sensitive information of a solid sample can be gained through several different techniques. In addition to PAS, ATR [57, 58], diffuse reflectance infrared Fourier transform (DRIFT) [59] and

confocal Raman spectroscopies [60] are capable of depth profiling layered materials to some extent. All of the above-mentioned techniques have a different physical and theoretical origin, which leads to different penetration depths in different scenarios. In ATR, the probing depth is determined by the internal reflection element material and the incident light angle [57]. In DRIFT, the sample is overlaid by a salt, such as KBr, and the thickness of this salt layer determines the probing depth [59]. In confocal Raman spectroscopy, the focusing plane of the microscope determines the depth [60]. Of course, the sample characteristics also affect the eventual penetration depth. In all cases besides PAS, the setup has to be modified somehow to achieve the different sampling depths. For achieving a different sampling depth in PAS, only the measurement parameters have to be changed, and both the sample and the setup can be left untouched. Also, PAS can collect simultaneous information from different layers by using the harmonics of the modulation frequency [61]. Furthermore, PAS is not sensitive to the morphology of the surface, is more selective to the sampling depth, and can be focused on small layers [62].

In PAS, the quantity that represents the sampling depth is the thermal diffusion length labeled as μ. The thermal diffusion length in the sample is determined by the thermal diffusivity of the sample and the modulation frequency [39]. In the RG-theory, thermal diffusivity α for material i is determined as

$$\alpha_i = \frac{k_i}{\rho_i C_i}, \tag{2.2}$$

where k_i, ρ_i, and C_i are the thermal conductivity, density and the specific heat of the material i, respectively. The thermal diffusion length (in material i) depends on this quantity by

$$\mu_i = \sqrt{\frac{2\alpha_i}{\omega}} = \sqrt{\frac{2k_i}{\omega\rho_i C_i}}, \tag{2.3}$$

where ω is the modulation frequency of the incident light beam. In this length, the thermal waves decay to 1/e (37%) of their original amplitude [42].

2.3 Optical cantilever microphone

The sensitivity in the photoacoustic detection can be improved by three factors: increasing the IR source intensity, cell optimization and microphone design. Clearly, the source intensity can only be improved in the

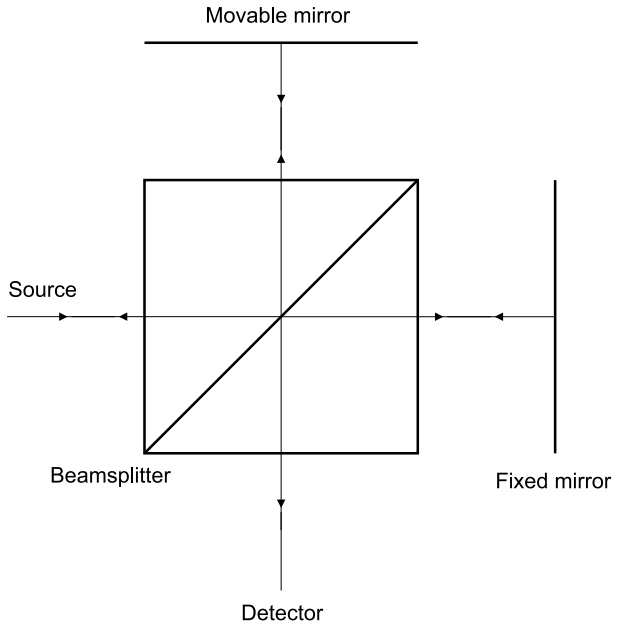

Figure 2.1: A Michelson type interferometer.

limits of the laser technology and compromises have to be made in the cell design to cover multiple applications. Thus, the element that truly limits the sensitivity of a photoacoustic system is the microphone.

In photoacoustic detection, condenser microphones are normally used as a pressure sensor. The condenser microphones already work near their theoretical limits, which means that the microphone needs to be redesigned if a considerable improvement in the sensitivity is desired. Well-established microphone improvements in PAS include a quartz tuning fork [63] and an optical cantilever microphone [11, 44]. Unlike quartz tuning forks, the optical cantilever does not require a resonance condition, which also makes it ideal for FTIR applications.

A typical cantilever microphone consists of a 5 to 10 µm–thick silicon cantilever and an interferometer to measure the position of the tip of the cantilever. Typically, the cantilever is gold coated for better reflectance. The interferometer can be of a Michelson or spatial construction. A Michelson interferometer is shown in Fig. 2.1. In a Michelson interferometer, a laser beam is guided through a beamsplitter and mirrors are placed at the end of each branch. These mirrors reflect the divided beams back to the beamsplitter, and the beams from different branches interfere. The

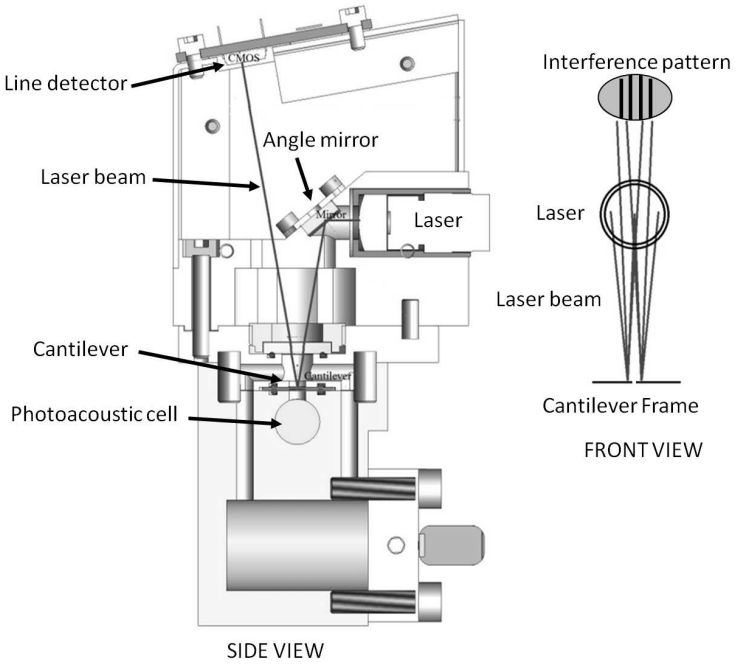

Figure 2.2: Photoacoustic cell with a spatial interferometer construction. The laser beam is split in half with a rooftop mirror. A CMOS array is used to detect the interference pattern of the beams originating from the cantilever and its frame. [Paper I]

intensity of the resulting beam can be controlled by altering the optical path difference (OPD) by moving one of the mirrors. In a Michelson construction, the cantilever works as the moving mirror of the interferometer. Contrary to FTIR, the beam returning to the source is also detected. The intensity of both source and detector branches are measured with photodiodes. A photoacoustic cell with a spatial interferometer construction is shown in Fig. 2.2. In spatial construction, the cantilever acts as a moving mirror and the cantilever frame as a fixed mirror. The laser beam is divided with an angle mirror. A complementary metal oxide semiconductor (CMOS) array is used to detect the interference pattern. The spatial construction is more robust and offers maintenance-free operation. Typically, Michelson interferometers are used in solid-phase, and spatial interferometers in gas-phase, applications. Dual-cantilever construction has also been introduced to enhance the vibration damping performance, which is crucial in the hand-held applications.

The cantilever and the membrane of the condenser behave differently in pressure variations: the cantilever only bends instead of stretching. Therefore, under the same pressure variation, the movement of the tip of the cantilever can be approximately two orders of magnitude larger than the movement of the middle point of the membrane [10, 11, 44, 45]. This is also experimentally verified [12]. Because the cantilever only bends, it is also superior in the dynamic range. In other words, while different condenser microphones have to be incorporated in measuring high or low pressure variations due to non-linearities in the microphone design, a single cantilever microphone can be constructed for an optimal performance in both. The dynamic range of a cantilever microphone is extremely large [10]. At present, there are cantilever-enhanced photoacoustic cells commercially available for both gas, and liquid or solid samples.

The dynamics and sources for noise of the optical cantilever microphone are well known and accurately modeled [11]. For a system where V and l are the volume and length of the sample cell, respectively, a_x and p_x are the absorption coefficient and the partial pressure of the absorbing gas, respectively, A_c, m, D, and ω_0 are the area, effective mass, damping factor, and resonance frequency of the cantilever, respectively, and P_0 is the maximum power and ω is the angular frequency of modulation of the infrared radiation, the total system response of the cantilever is

$$A(\omega) = \frac{A_c(\kappa-1)}{V} \frac{a_x p_x l P_0}{m\sqrt{(\omega_0^2-\omega^2)^2 + (\frac{\omega D}{m})^2}} \times \frac{\tau_1}{\sqrt{1+(\omega\tau_1)^2}} \frac{\omega\tau_{23}}{\sqrt{1+(\omega\tau_{23})^2}} \frac{1}{\sqrt{1+(\omega\tau_4)^2}}, \tag{2.4}$$

where $\kappa = C_p/C_V$ is the ratio of specific heat capacities: C_p for constant pressure and C_V constant volume, τ_1 and τ_{23} are characteristic time constants, where $\tau_1 = C_V/G$ and G is the total thermal conductivity of the gas content inside the cell and $\tau_{23} = (\frac{3A_g}{4\sqrt{\kappa}V_{eff}}\nu_{sound})^{-1}$, where A_g is the area of the gap between the cantilever and its frame, $V_{eff} = (\frac{1}{V} + \frac{1}{V_0})^{-1}$, where V_0 is the volume at the rear of the cantilever and ν_{sound} is the speed of sound in the gas, and τ_4 is the effective relaxation constant. The derivation of the Eq. 2.4 and the assumptions made during the derivation can be found in Ref. 11.

The term $\frac{\tau_1}{\sqrt{1+(\omega\tau_1)^2}}$ appears due to the heating of the sample gas and acts like a low-pass filter. The term $\frac{\omega\tau_{23}}{\sqrt{1+(\omega\tau_{23})^2}}$ acts as a high-pass filter in the system, and represents a combination of two processes that appear

due to the gap between the cantilever and the frame. The processes are gas flow, due to pressure difference, and energy transfer, due to temperature difference. The processes share a similar characteristic time scale and therefore can be combined. The term $\frac{1}{\sqrt{1+(\omega\tau_4)^2}}$ acts as a low-pass filter and represents the non-radiative relaxation pathways. Although the pathways and energy levels are complex, the total relaxation process can be modeled with only one effective constant. Typically the relaxation times are less than 1 ms [11].

Cantilever operation has four noise sources: acceleration noise, acoustical noise, Brownian noise and electrical noise. The acceleration noise is generated by the coupling of the external disturbances to the cantilever. Typically, these are low-frequency vibrations that couple to the support structure and thus to the cantilever. This is different to the acoustical noise, which is generated by external acoustical waves that are leaked into the sample cell. Brownian noise appears due to the random collisions of the gas molecules and the cantilever. Brownian noise is the noise type that ultimately limits the operation of the cantilever. Electrical noise originates from various components in the sensor system. Normally, electrical noise is lower than other noise types in cantilever-based photoacoustic detection [11].

2.4 FTIR photoacoustic spectroscopy

FTIR spectrometers have received a wide acceptance since their introduction, and are the standard work horses in IR laboratories. The factor that discriminates FTIR devices from any other spectrometer type is that all the wavelengths are collected simultaneously. This, combined with the high throughput of FTIR devices, makes them superior in performance than the other types of IR spectrometers [64]. The operation of an FTIR device rests upon a simple Michelson type interferometer, shown in Fig. 2.1, or its derivative. The information of the intensity at different positions of the moving mirror is the source of spectral information in the FTIR spectrometer [65, 66]. A Fourier transform is applied to this data to transfer from spatial coordinates to frequency, or more commonly wavenumber coordinates. The operation of FTIR spectrometers is well known and the sources for error have been carefully modeled over the past decades. A thorough review of FTIR instruments and Fourier transforms in spectroscopy can be found in Refs. 65 and 66.

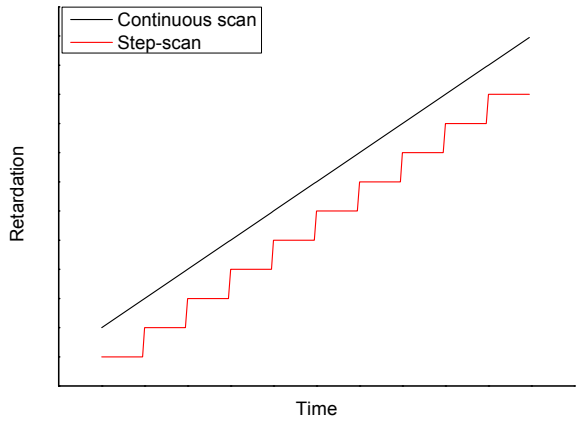

Figure 2.3: The mirror movement in continuous and step-scan.

Table 2.1: Modulation frequency in different parts of the spectrum for 2.2 kHz FTIR scan velocity.

ν (cm^{-1})	400	800	1200	1600	2000	2400	2800	3200	3600	4000
f (Hz)	56	111	167	223	278	334	390	445	501	557

2.4.1 Rapid-scan and step-scan

Continuous scan or rapid-scan is the usual way to perform an FTIR measurement. Rapid-scan accounts for mirror velocities usually greater than 0.1 mm/s, which is a common condition for almost all FTIR spectrometers. In rapid-scan, the moving mirror travels at a constant velocity, until it reaches the maximum desired optical retardation and is retraced back to its starting point. The intensity of the interferogram is read at constant intervals of the mirror position. The position of the mirror can be read from both directions, or only the forward direction, of the mirror [65]. The retardation for the rapid-scan is shown in Fig. 2.3. Usually, multiple scans are co-added for a better signal-to-noise ratio (SNR). Because the measurement noise is random by nature, SNR increases in the square root of the number of scans [67].

However, rapid-scan is not the best selection for photoacoustic detection

due to the varying modulation frequency with different wavelengths. The speed of the moving mirror and the wavelength of the radiation determine the actual modulation frequency [64]. FTIR modulation frequency is given as

$$f = f_{laser}\frac{\nu}{\nu_{laser}}, \tag{2.5}$$

where ν is wavenumber, f_{laser} is the scan velocity in respect to laser frequency and ν_{laser} is the wavenumber of the laser. The typical wavenumber of the HeNe-laser in the FTIR spectrometers is 15800 cm^{-1} (632.8 nm) [65].

A step-scan mode is usually found in the higher-priced spectrometers or it can be purchased as an accessory. In the step-scan mode, the moving mirror travels to a desired location and stops before the acquisition of the data. In step-scan FTIR-PAS, a separate source for modulation has to be included. The retardation in step-scan is shown in Fig. 2.3. Fig. 2.3 shows a single scan with both rapid-scan and step-scan modes. However, in practice multiple rapid-scan spectra are collected, as step-scan is considerably slower in measurement time. In a step-scan measurement, usually only one scan is collected, but the data are signal-averaged at each step of the mirror [65]. There are two ways to execute a step-scan. The first is to perform it exactly as defined above and stop the mirror for collecting each data point in the interferogram. However, this induces mechanic vibrations in the mirror, and a certain time has to pass before the mirror is again stable. This is a necessary condition to achieve a good repeatability and SNR. The other possibility is to introduce two moving mirrors; that is, to also move the fixed mirror. The principal moving mirror is moved forward at a constant velocity. Simultaneously, the fixed mirror is moved with the same velocity in the reverse direction, keeping the resulting optical retardation constant. Then, the fixed mirror is moved rapidly to its original starting position resulting in a step in the optical retardation. The small movements of the fixed mirror are performed with piezoelectric actuators, which allow the interferometer to settle rapidly. In this construction, no time is spent in the stabilization of the vibrations. Fig. 2.4 shows the resultant optical retardation and movement of each mirror in the latter case. In the step-scan mode, the harmonics of the modulation frequency can also be collected simultaneously, and therefore it is possible to perform photoacoustic depth profiling analysis based only on a single measurement [8, 61].

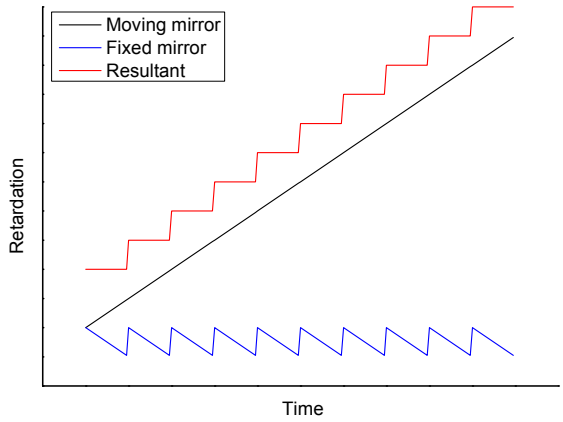

Figure 2.4: An alternative way to perform a step-scan: both mirrors are constantly moving and the steps are generated in the resultant optical retardation.

2.5 Photoacoustic laser spectroscopy

Multiple laser constructions, such as diode or quantum cascade, can be used in conjunction with photoacoustic detection. In addition, OPOs can be used in a similar fashion. Lasers are usually applied in gas-phase PAS, but lately the number of studies with solids has also started to increase [1, 68–70].

2.5.1 Benefits of lasers to FTIR

There are some clear advantages of using tunable lasers over the standard FTIR spectrometers. The first obvious advantage is the high spectral power density. In an FTIR measurement, the lowest sufficient resolution should be used for an optimal SNR. The reason is that the SNR increases linearly when the resolution is lowered [42]. In a laser measurement, the optical power per a single data point in the spectrum is unconnected to the used resolution, which provides a benefit when measuring high-resolution spectra. This advantage is lost if low resolution is sufficient for the measurement. High-resolution spectra are usually needed in gas-phase measurements. The resolution used also limits the aperture size of the FTIR

instrument. A fully open aperture cannot be used with the highest resolutions, which dramatically lowers the SNR.

In an FTIR instrument, the measured range of wavelengths cannot be narrowed for a faster measurement as all the wavelengths are collected simultaneously. In a laser measurement, all wavelengths are independently collected. This enables, for example, the possibility to concentrate all available measurement time to measure only the important regions or peaks in the spectrum as accurately as possible. In practice, this can be used for obtaining a higher detection limit or SNR. In some sources, this is called an inverse multiplex advantage [71].

There are also benefits particularly related to solid samples. With conventional FTIR devices, there are optical limits for how small the focused image of the source could be, and making the beam size smaller means high attenuation in the optical power. In contrast, the laser beam can be imaged down to a small spot without losses in throughput due to its point source nature. This results in several times higher spectral radiance. In practice, the spectral radiance of, for example, a QCL source can be as much as seven orders of magnitude higher than that of the FTIR source. Another benefit relates to the modulation frequency. In a rapid-scan FTIR measurement, the modulation frequency rises linearly when moving from low to high wavenumbers due to the way the data collection is performed. In the mid-IR (400–4000 cm^{-1}), which is typically used in FTIR measurements, this results as a 10-fold difference in the modulation between the extremes. In PAS, this means that the signal comes from the different depth in the sample in the different parts of the spectrum. The thermal diffusion length is inversely proportional to the square root of the modulation frequency, which results in a 3-fold thermal diffusion length in the lowest wavenumbers. This complicates the depth profiling of solid samples. In a laser measurement, the modulation is usually performed electrically by altering the current of the chip, or mechanically with an optical chopper. In both cases, the modulation frequency does not depend on the wavelength of the source, and a constant modulation can be achieved in all parts of the spectrum. Of course, this problem can also be overcome by using step-scan FTIR-PAS.

Novel lasers can operate without extensive water-cooling systems and high-resolution devices can be crafted to have a small overall size. In contrast, the maximum resolution of a FTIR spectrometer depends on the size of the interferometer, which means that high-resolution devices cannot be constructed in a small size. The drawbacks of the lasers are related to the

comparison of grating and FTIR spectrometers, but without the benefits of lasers in the optical power and resolution. Currently, the tuning of the lasers is generally slower than the FTIR operation, and scanning the full range takes significantly more time than one scan of the FTIR spectrometer. Also, the available tuning ranges of the present lasers cannot compete with the tuning range of FTIR spectrometers.

2.5.2 Quantum cascade laser

The QCLs of today have convenient attributes such as high optical power, tunability and narrow line width [13, 47]. Furthermore, they can be constructed in a relatively small size and can be operated at room temperature by using thermo-electrical cooling (TEC). In QCL operation, electrons undergo quantum jumps between energy levels to create laser photons. Electrons are not consumed in the emission of a laser photon and can be recycled to emit another photon. The high power of QCLs is a resultant of this cascading effect [13].

QCLs can be constructed to operate at any wavelength between 3 and 24 µm [47]. The corresponding range in wavenumbers is 3300–400 cm^{-1}, which is most of the mid-IR region. Single frequency operation is achieved by introducing a distributed feedback (DFB) structure. Typically, the maximum tuning range of a DFB-QCL that can be achieved by altering the current of the chip is 3–4 cm^{-1}. This can be extended to about 20 cm^{-1} by altering the temperature in addition to the current [47]. The line width of a QCL is normally between 0.01 and 0.001 cm^{-1} [13, 47]. The wavelength coverage can be further broadened by using an array of QCLs [14]. However, this design suffers notably from the different characteristics of the independent lasers.

2.5.3 External cavity quantum cascade laser

Although DFB-QCLs can reach a maximum tuning range of 20 cm^{-1}, the actual gain profile of a QCL is normally notably wider [47]. Another way to achieve the single frequency operation with a QCL is by including an EC. The EC-QCL design consists of three main components: the gain element (QCL chip), the collimating lens and the grating that acts as a wavelength filter [14]. The drawback of the EC design is the broadening of the laser line width due to the dispersion in the diffraction grating. The line width of an EC-QCL is typically less than 1 cm^{-1}. Tuning ranges for over 250 cm^{-1} in mid-IR region can be achieved with a single EC-QCL. Also,

multiple EC-QCL units can be multiplexed into the same beam path to cover an even broader tuning range. The latest designs can achieve a tuning range of over 1000 cm^{-1} with a single collimated laser beam. This enables the broadband spectroscopy of large molecules, which has previously been limited to standard FTIR spectrometers.

The EC-QCLs can operate in either a continuous or pulsed mode and CEPAS can be used for both modes. Continuous wave (CW) operation yields considerably higher output powers but can require water cooling. A pulsed mode enables broader tuning ranges but the resolution suffers. In the pulsed operation, the laser line width is broadened by the competing laser modes due to the electrical chirp of each laser pulse. In this study, the use of pulsed mode operation appears to be more promising for its broader tuning ranges.

Fig. 2.5 shows a typical EC-QCL setup for measuring solid samples with CEPAS. A broadband QCL chip is placed between the collimating output and cavity lenses. The EC is of Littrow configuration with back extraction, which means that the output beam is on the opposite side. A rotating grating is used to select the wavelength of the QCL. Diffracted light from the grating couples back into the QLC chip, creating the laser output. The wavelength (single wavelength only in an ideal case) of the laser output depends on the position of the grating. The EC-QCL is electronically modulated by altering the current of the QCL chip. The modulated laser beam is guided into the photoacoustic cell with an adjustable plane mirror and targeted at the sample with a focusing mirror. An optical cantilever microphone is then used for the detection of the acoustic signal in the photoacoustic cell.

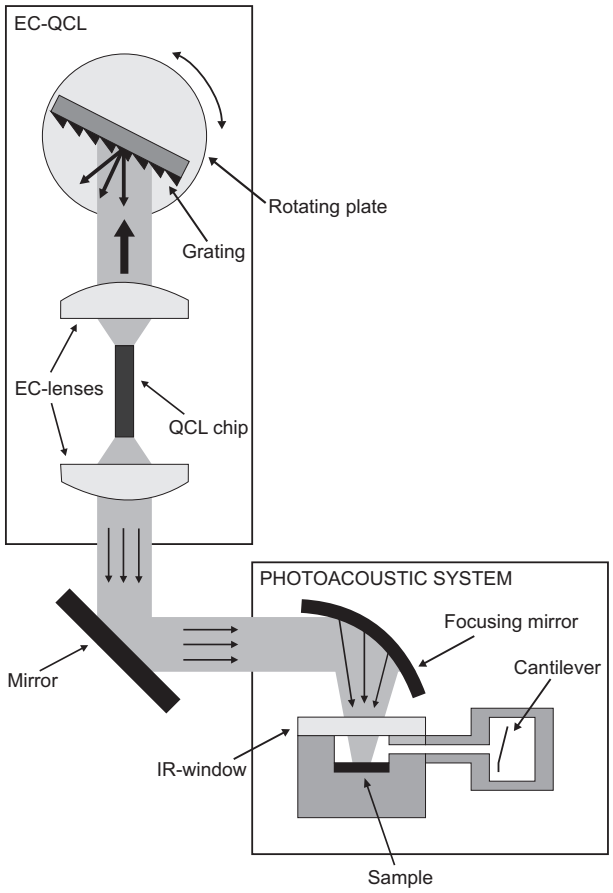

Figure 2.5: EC-QCL photoacoustic setup. The operating wavelength of the EC-QCL is selected by the alignment of the grating. An adjustable mirror is used to guide the laser beam into the photoacoustic detector, whereas another mirror is used to focus the beam on the sample cell. [Paper VI]

Chapter 3

Cantilever-enhanced photoacoustic spectroscopy of gas- and solid-phase samples

3.1 Photoacoustic detection of formaldehyde

An obvious application of PAS in the gas-phase is a single component study, where high optical power is concentrated in a small spectral range for a low detection limit. Extremely low detection limits are needed in the monitoring of highly toxic or hazardous components. In this study, formaldehyde (HCHO) was measured with the QCL-PAS setup illustrated in Fig. 3.1. Formaldehyde is widely used in industry, for example in the production of resins and plastics. Formaldehyde is toxic, mutagen and possibly carcinogenic. Therefore, formaldehyde is monitored in its industrial use but also in indoor and outdoor air, due to the various sources of it, such as wood combustion, laminates and coatings [72].

The setup combined a PA201 cantilever-enhanced photoacoustic detector (Gasera, Ltd.) and a DFB-QCL (III–V lab), which was tunable over 1772–1777 cm^{-1}. A more comprehensive description of the used equipment and the experimental procedures is in Paper II. Formaldehyde is a small molecule with sharp spectral peaks, so the relatively small tuning range of the used QCL is sufficient. The measurements were performed in an underpressure of 350 mbar for even sharper spectral peaks and minimal overlap. The used resolution was 0.018 cm^{-1}. In this case, the resolution corresponds to the tuning steps of the laser. A tuning fork operating at 135 Hz was used as the modulation element. Also, wavelength modula-

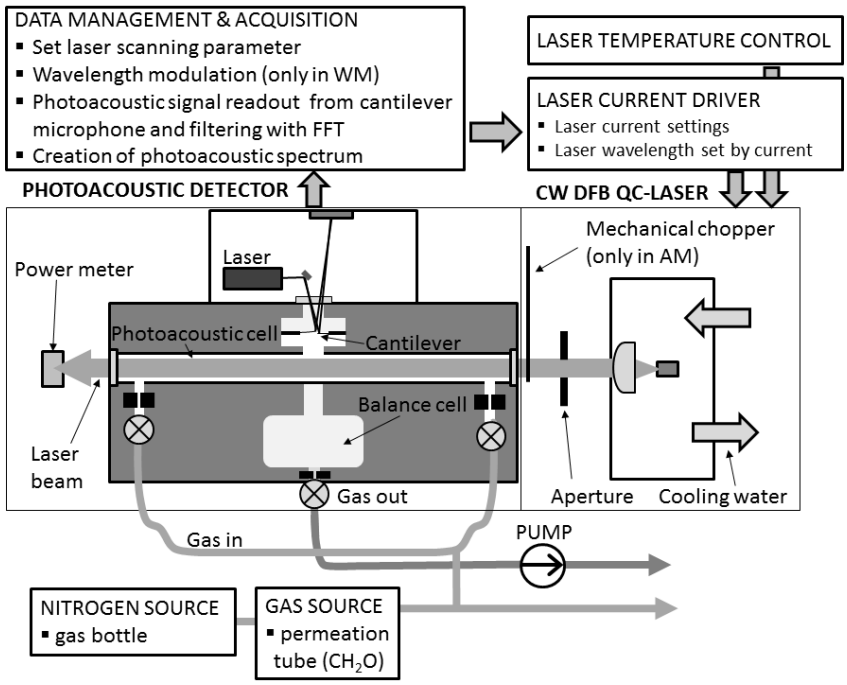

Figure 3.1: Schematic of the LPAS setup to measure formaldehyde. [Paper II]

tion (WM) at 70 Hz was utilized in the place of the mechanical amplitude modulation (AM). WM was performed by altering the current of the QCL chip. A 2 ppm mixture of formaldehyde was generated using a FlexStream permeation tube system (KIN-TEK Laboratories, Inc). The permeated formaldehyde was diluted into a nitrogen flow in a constant temperature and flow for a controlled concentration. The 2 ppm target concentration was used in the permeation tube system to ensure sufficient flow to maintain a stable concentration of formaldehyde.

The measured AM photoacoustic spectrum of formaldehyde is shown in Fig. 3.2. The negative features in the spectrum appear due to inaccuracy in the subtraction of the water spectrum. The nitrogen background was measured over a 2 min measurement time to discover the noise characteristics of the used setup in AM. Fig. 3.3 shows the measured photoacoustic signal for a 2.8 mW laser current. The signal has a form of a rising slope due to the water desorption from the cell walls. To be able to characterize the noise in the photoacoustic detection, this slope has to be removed. To do this, fourth-order polynomial fit was subtracted from the measurement

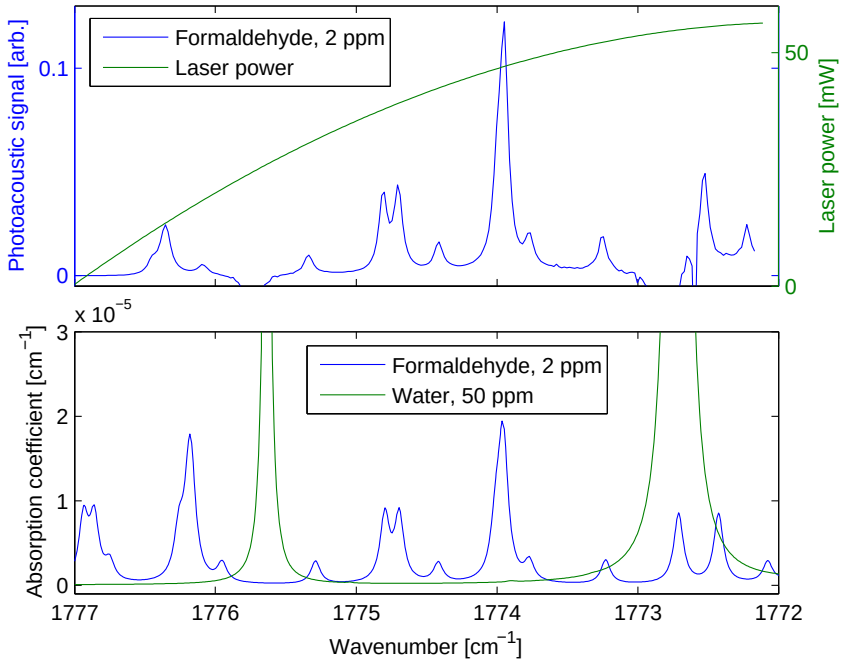

Figure 3.2: *Upper graph:* measured amplitude modulated formaldehyde spectrum at 2 ppm, and the laser power emission curve. The spectrum of formaldehyde contains negative elements, which are residuals of the water subtraction. *Lower graph:* absorption coefficient of 2 ppm formaldehyde and 50 ppm water at 350 mbar and 323.15 K, modeled with HITRAN [73]. [Paper II]

data. Fig. 3.3 shows the signal before and after the subtraction of the slope. After the subtraction, RMS noise could be calculated. In practice, the RMS noise is the standard deviation of the noise signal [67]. Twelve sets of standard deviations from ten successive data points were calculated and averaged for a final estimation of the noise. The calculated detection limit (3 x RMS) was 1.6 particles per billion (ppb) in 0.951 s using AM. The detection limit was calculated for the 1773.959 cm^{-1} peak and the laser power was 47 mW at that point. Even a lower detection limit of 1.3 ppb for the same peak was achieved with the WM. The parameters used in the calculation are shown in Paper II. The achieved detection limits are notably lower than the occupational health limit for formaldehyde in Finland (300 ppb) [74], polluted indoor conditions (80–300 ppb), normal indoor conditions (10–80 ppb), and normal outdoor conditions in urban areas (3–25 ppb) [72]. Therefore, the setup used in this study could readily be used in

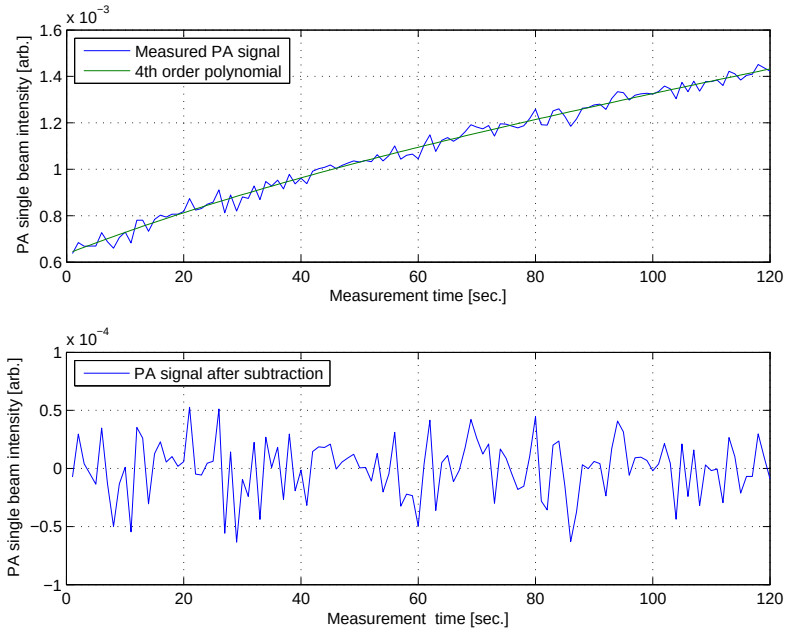

Figure 3.3: *Upper graph:* one example of time series of the photoacoustic signal of nitrogen (recorded at 450 mA laser current and 2.8 mW laser power) and its fourth-order polynomial fit. The signal increase over time is due to desorption of water from the cell interior. *Lower graph:* nitrogen signal after subtraction of the fit. [Paper II]

practical applications requiring accurate monitoring of formaldehyde.

3.2 Photoacoustic FTIR spectroscopy of human hair

Hair has been a problematic sample material for IR spectroscopy. Normally, it has been studied using ATR or DRIFT spectroscopy, but the sample preparation methods can lead to problems in reproducibility [75]. In addition, studies with individual hair fibers have suffered from low sensitivity and sampling problems. Photoacoustic spectroscopy is a valuable tool for studying hair fibers due to its high sensitivity and microsampling capabilities [76]. Hair has been investigated by PAS in several previous studies [75–78]. In general, hair is of interest to investigations, as it can be

used as a matrix in multiple purposes, for example in monitoring diseases [79], drugs of abuse [4, 27, 28, 31, 32], chemical treatments and weathering [80–82] or even malnutrition [30, 83].

3.2.1 Structure and chemical composition of hair

Three different layers in the hair structure can be discerned: the cuticle, the cortex, and the medulla [30, 84]. The cuticle is the protective and chemically resistant outermost layer in hair. The cuticle consists of 5 to 10 layers of overlapping flat cells. The overall diameter of the cuticle is approximately 5 µm. Furthermore, the cuticle cells have a fine structure and consist of differing layers. The cortex is composed of long cells and intercellular binding material. The cortex contains most of the overall mass in a hair fiber [30]. The average diameter of the cortex is 40 to 60 µm [57]. Inside the cortical cells, a similar structure of macrofibrils can be found. Furthermore, inside the macrofibrils is a structure of microfibrils and surrounding matrix material [30]. Finally, inside the microfibril, polypeptide chains of proteins are found in different formations such as helices, sheets and turns [30, 85, 86]. The different formations of the cortex polypeptide chains can be examined with IR spectroscopy as the different formations produce vibrations in different wavenumbers in mid-IR [87, 88]. Unlike in the cuticle, the structure of the cortex is highly organized at the molecular level. In the core of the hair fiber is the medulla. The medulla can be completely absent, continuous along the fiber axis, or discontinuous. The medulla consists of loosely packed, hollow, spherical cells bound together by an intermediate material, and contributes only a small part of the fiber mass [30]. The average diameter of the medulla is 5 to 10 µm [57]. The diameters of different layers, as well as the overall diameter, vary substantially between different individuals. Therefore, the diameter of a human hair fiber can be from 30 to 120 µm [30].

Hair mostly consists of long fibrous proteins that are generally called keratin [30, 84]. The protein content in hair is 65–95 % depending on the moisture content. The proteins are long chains of various amino acids that can be converted to their derivatives as a result of chemical treatments or weathering. Other components include water, lipids, pigment and trace elements. The lipid in human hair is comprised of an external surface lipid and internal lipid [30]. The internal lipid can either be a free lipid or structural lipid [30, 89]. The lipid content originates from the sebaceous glands of the scalp. Much of the surface lipid is removed by washing the

hair. The lipid content is less than 10 % of the total mass. Pigment in human hair consists of brown-black eumelanins and red pheomelanins. Eumelanins are more significant in the hair pigment and are usually called simply melanins. The pigment granules can be found in the cortex and the medulla, and constitute a maximum of 3 % of the total fiber mass. Trace elements comprise less than 1 % of the total mass. The inorganic content in hair can be of interest in medical and forensic examinations [30].

3.2.2 Photoacoustic spectroscopy of hair samples

The cuticle and the cortex are the regions that can be reached with normal rapid-scan FTIR-PAS due to the relatively high modulation frequencies available in a typical FTIR spectrometer. With step-scan FTIR-PAS or another techniques using external modulation, medulla can also be examined. Table 3.1 shows the thermal diffusion lengths in hair at different parts of the spectrum calculated for several FTIR scan velocities. The absolute differences in the thermal diffusion length due to the FTIR data acquisition are clearly more pronounced at lower scan velocities.

A composition of individual hair fibers was measured with a Tensor 37 (Bruker Optics, Inc.) FTIR spectrometer and a PA301 cantilever-enhanced photoacoustic detector (Gasera, Ltd.). Hair fibers were cut into approximately 2 mm pieces, and laid on the bottom of the sample cup. The parameters used in the measurement were: an 8 cm^{-1} resolution, 20 scans, and a 5 kHz scan velocity. The photoacoustic cell and the sample cell were purged with helium before the measurements for an enhanced signal and carbon black was used in the normalization of the spectrum. Helium is also used as a carrier gas and carbon black also used for normalization in the following solid-phase experiments of this study. Fig. 3.4 shows the measured photoacoustic mid-IR spectrum of hair, and the different vibrations in the spectrum are explained. The vibrations of amide bonds dominate the spectrum of hair. Five different vibration bands of the amide bond are found in the mid-IR region, namely amide A, B, I, II, and III. The N–H stretching vibration of the amide bond gives rise to Amide A and B bands that appear at 3300 cm^{-1} and 3170 cm^{-1}, respectively. Amide I appears at 1650 cm^{-1} and is the strongest individual feature in the spectrum of hair. The amide I band consists mainly of C=O stretching vibration with contributions from the C–N stretching and N–H bend. The amide II band appears at 1550 cm^{-1} and consists mainly of a combination of the N–H bend and C–N stretching. A combination of N–H bend and C–N stretch-

Table 3.1: Thermal diffusion length (in µm) in hair for several FTIR scan velocities.

ν	FTIR scan velocity					
(cm^{-1})	100 Hz	500 Hz	1 kHz	2.2 kHz	5 kHz	10 kHz
4000	16.3	7.3	5.2	3.5	2.3	1.6
3600	17.2	7.7	5.4	3.7	2.4	1.7
3200	18.2	8.1	5.8	3.9	2.6	1.8
2800	19.5	8.7	6.2	4.2	2.8	1.9
2400	21.0	9.4	6.7	4.5	3.0	2.1
2000	23.0	10.3	7.3	4.9	3.3	2.3
1600	25.8	11.5	8.1	5.5	3.6	2.6
1200	29.7	13.3	9.4	6.3	4.2	3.0
800	36.4	16.3	11.5	7.8	5.2	3.6
400	51.5	23.0	16.3	11.0	7.3	5.2

The constants used for the calculation of the thermal diffusion lengths were $k = 9.0531 \cdot 10^{-5}$ cal$\cdot\,^{\circ}C^{-1}\cdot s^{-1}\cdot cm^{-1}$, $\rho = 1.32$ g$\cdot cm^{-3}$ and $c = 0.325$ cal$\cdot g^{-1}\cdot\,^{\circ}C^{-1}$. The constants are for wool, but the appropriate constants for human hair are essentially the same [75].

ing also constitutes the Amide III that appears around 1240 cm^{-1} [87, 88]. Methylene group (CH_2) and methyl group (CH_3) vibrations appear in two different wavelength areas in the spectrum. Symmetric and asymmetric stretching of CH_2 and CH_3 appear in 2850–3000 cm^{-1} and symmetric and asymmetric bending in 1350–1480 cm^{-1}. These vibrations arise from the long CH–chains of the lipids and also from the CH_2 and CH_3 groups of proteins [88]. Other notable features are water, and cystine and cysteine derivatives. The O–H stretching vibration of bonded water appears as a broad shape under the amide A and B peaks between 3000 and 3700 cm^{-1}. The different vibrations of the S=O bond of cysteic acid and cystine oxidation products appear between 1020 and 1220 cm^{-1}. These include, for example, cysteic acid (1219 cm^{-1}), cystine mono- (1071 cm^{-1}) and dioxide (1121 cm^{-1}), sulfonate (1040 cm^{-1}) and Bunte salt (1022 cm^{-1}) [30, 81, 82]. Most derivative or degradation products of amino acids are derivatives of cystine. Cystine is the most investigated individual amino acid due to its high reactivity and high concentration in hair [30].

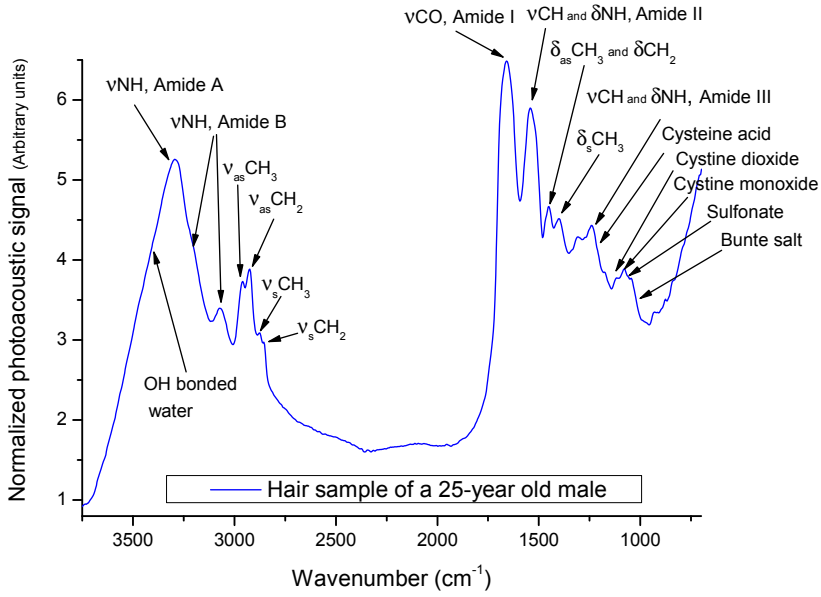

Figure 3.4: The individual vibrations in the photoacoustic mid-IR spectrum of a hair sample explained.

The different protein formations mentioned in the previous section can be observed in the fine structure of amide I, II, and III bands [85, 86, 90]. Also, the side chains of the individual amino acids have an effect on the shape of the amide bands [91, 92]. Fig. 3.5 shows a simple depth profiling experiment conducted originally in Paper III. Differences in protein formations between the different layers of hair were observed when measuring the same hair sample with different scan velocities. The sample was measured with 2.2 kHz and 10 kHz scan velocities. Due to Eq. 2.3, the thermal diffusion length varies with a factor of 2.13 between the two scan velocities. According to Table 3.1, the thermal diffusion length in the mid-IR region is 3.5–11 µm for a 2.2 kHz scan velocity and 1.6–5.2 µm for a 10 kHz scan velocity. In practice, this means that for a 2.2 kHz scan velocity, the signal comes from the cuticle and cortex, while for a 10 kHz scan velocity the signal comes solely from the cuticle. Fig. 3.5 shows the measured spectra for both scan velocities and the 2.2 kHz spectrum treated with a saturation compensation algorithm. The saturation compensation algorithm demonstrated by McClelland et al. [42] was applied to transform between different optical velocities. Saturation compensation

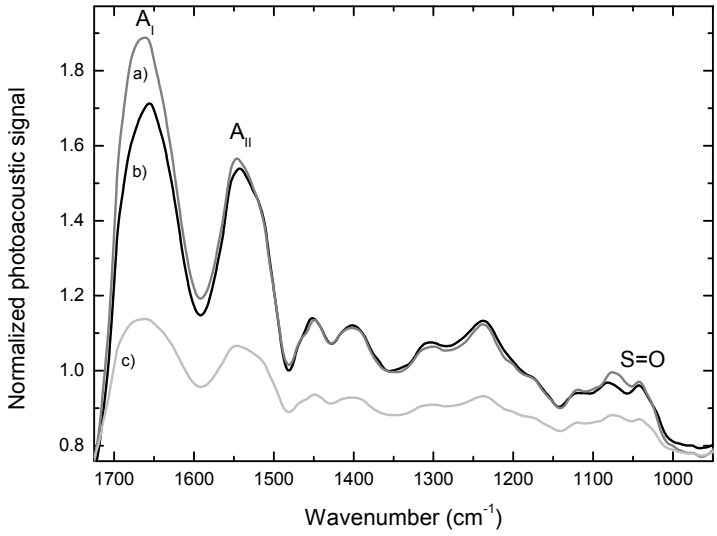

Figure 3.5: A simple approach to depth profiling. A spectrum of the same hair sample is shown with three different configurations: (a) 2.2 kHz spectrum with saturation compensation, (b) 10 kHz spectrum, and (c) 2.2 kHz without saturation compensation. The amide I and II peaks shift to lower wavenumbers as the scan velocity is increased. [Paper III]

or linearization algorithms are generally used to remove the saturation differences while retaining any differences related to sample structure [8, 42]. When the scan velocity is increased, the bands that are saturated increase relative to the weaker bands, due to the reduction of the saturation effects [42]. The use of linearization or saturation compensation algorithms is important in hair samples, where the photoacoustic signal is mostly nonzero. This means that some level of saturation can be found all over the spectrum. This simple saturation compensation algorithm only applies to a magnitude spectrum, whereas linearization methods use both phase and magnitude spectra [8, 42]. In Fig. 3.5, we can see that the spectra of hair samples with radically different mirror velocities are basically incomparable before the saturation compensation.

If we compare the compensated spectra, we first see the differences in the amide I peak at 1655 cm^{-1}, which are mainly due to saturation effects, as the amide I peak can often be out of the linear range of Beer's law.

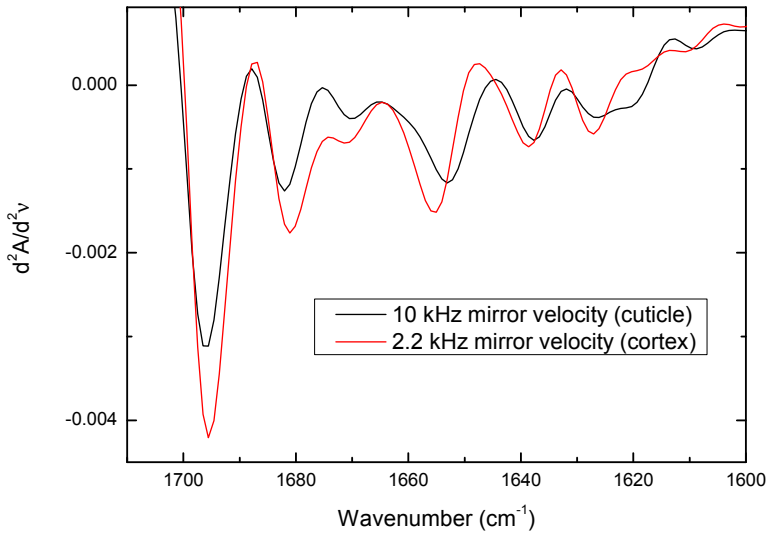

Figure 3.6: Second derivative of the amide I band obtained for both scan velocities. Differences in the peak positions occur due to the different protein formations and amino acid composition between the different layers.

This has also been noted in previous studies with hair samples [75, 81, 93]. However, we found differences in the positions of the maxima of the amide I and II peaks, which is an actual feature. The amide I and II peak maxima shift to lower wavenumbers as the scan velocity is increased due to changes in the shape of the amide bands. The shift is approximately 8 cm^{-1} for the amide I peak and 4 cm^{-1} for the amide II peak. This relates mainly to the differences in protein formations between the different layers but also has a minor contribution from individual amino acid side chains [85]. Moreover, differences in the spectra between 1000–1100 cm^{-1} can be observed. This is due to the weathering of the cuticle, for example due to shampoo washing and combing the hair, and exposure to sunlight [80–82]. With the 10 kHz scan velocity, the ratio of the 1042 cm^{-1} and 1076 cm^{-1} peaks has risen due to the increased amount of S=O bonds present. The S=O bond appears due to the oxidation and can be assigned to sulfonate or sulfonic acid groups [81, 82].

A second derivative is usually applied to distinguish between the overlapping spectral features. Generally, a smooth spectrum with a good SNR

is needed for a reasonable calculation of the derivatives. Although the resolution used was 8 cm^{-1}, the data points were at 1 cm^{-1} intervals due to zero filling. Also, the amide I peak was the highest intensity feature with a high SNR in both spectra. The second derivative of the amide I band was calculated for both scan velocities. Fig. 3.6 indeed shows the differences in the fine structure. Most peaks appear in slightly different wavenumbers in the two spectra. In the amide I band, these peaks mainly belong to β–sheet and β–turn formations [85]. Further, a peak centered around 1620 cm^{-1} that is weak in the 2.2 kHz spectrum is more prominent in the 10 kHz spectrum. Bands in the region of 1620–1640 cm^{-1} have been assigned to β–sheet formation by many authors [85]. Also, amino acids lysine and tyrosine are active around 1620 cm^{-1} [92]. However, no simple correlation between the IR spectra and the secondary structure can be drawn.

3.2.3 Studies with other keratins and proteins

Two different hair samples, a nail sample and a saliva sample were measured with an FTIR-PAS setup. The first hair sample was a composition of hair fibers and the second was a single 1 cm piece of hair. A modified Nicolet Antaris IGS Analyzer (Thermo Scientific) FTIR spectrometer and the PA301 photoacoustic detector were used in the measurements with an 8 cm^{-1} resolution, 20 scans (100 scans for the single fiber), and a 2.5 kHz scan velocity. In Fig. 3.7, the photoacoustic spectra for different types of proteins are shown. Fingernails consist of similar keratin as hair fibers. Fingernails are composed of three different layers of keratin lying on the top of the nail bed [94]. Saliva is a complex mixture of proteins and other molecules originating from different sources. It consists mostly of water, proteins and inorganic and trace substances, and contains more than 1000 peptides or proteins [95]. Unlike the proteins in hair and nail, salivary proteins are different from keratin. In this study, the saliva sample was dried before the measurement. This was done to prevent the cell windows from deteriorating. Although the dried sample consisted of only a thin layer, a spectrum with a high SNR could be measured. The four spectra show similar features, and the spectral assignments above can be applied for each spectrum in Fig. 3.7. The only clear difference between the spectra is the 2058 cm^{-1} peak in the spectrum of saliva, which belongs to the antibacterial compound thiocyanate (SCN^-) [96]. Other than that, the differences relate mostly to the peak shapes and relative intensities. Again, the different shapes of the amide bands are related to the different protein structures and

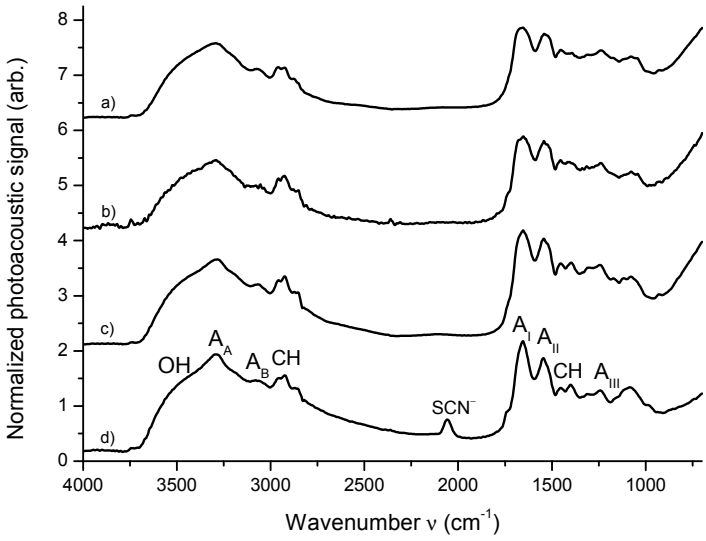

Figure 3.7: Different types of keratin, and saliva proteins measured with FTIR-PAS. Photoacoustic signal was normalized with a carbon black sample and is shown in arbitrary units: (a) a hair sample (composition), (b) a hair sample (single fiber), (c) a fingernail sample, and (d) a saliva sample. Notations A_A, A_B, A_I, A_{II}, and A_{III} in the figure represent amide A, B, I, II, and III peaks, respectively. The symbol CH represents CH_2 and CH_3 peaks of lipids and fatty acids and OH signifies bonded water in the spectra. [Paper III]

different amino acid compositions. The basic building blocks of the samples are the same but with varying ratios of different components. More details can be found in Paper III. Since the spectra of different proteins appear to be essentially similar, it is possible to expand the results and knowledge of hair to other keratin and protein sources. For example, this could include numerous applications of photoacoustic IR spectroscopy with skin [97, 98].

3.2.4 Microsampling techniques in photoacoustic detection

Photoacoustic spectroscopy, as infrared spectroscopy in general, is capable of measuring physically small sample sizes. However, in small samples, normal sampling and measurement procedures do not generally apply, and

different sampling techniques have to be introduced for an adequate SNR. In PAS, these kinds of samples are often called as microsamples [8, 76, 99]. Typical microsamples are, for example, single fibers or single particles. In Paper V, hair microsamples were considered. The dimensions of these particles can be as small as tens of micrometers. The effect that is often encountered in an FTIR-PAS measurement of microsamples with regular sampling relates to the basics of the photoacoustic effect. If a small particle is placed at the bottom of the photoacoustic cell and radiated with an IR source, the heat does not transfer into the surrounding gas but instead is converged into the bottom of the photoacoustic cell, i.e., the sample cup. From the RG-theory, one finds that the thermal boundary layer of the surrounding gas is $2\pi\mu$, where the thermal diffusion length μ depends on the modulation frequency and the properties of the sample according to Eq. 2.3. Therefore, the effect is reduced if the scan velocity, and thus the modulation frequency, is increased. However, it cannot be completely eliminated as the sample is in direct contact with the sample cup. Moreover, the photoacoustic signal intensity decreases when the modulation frequency is increased. This is undesirable in microsamples, as the signal intensity is often initially low, and cannot be compromised.

A solution, which prevents the heat from converging into the photoacoustic cell, is to elevate the sample above the surface of the sample cup. The height of the sample should be at least equal to the thickness of the boundary layer. There are a couple of solutions for this for different types of microsamples [99]. A tungsten needle can be used to elevate small particles; then, only the tip of the sharp needle is in direct contact with the sample, and most of the heat is transferred into the surrounding gas. The electrostatic force between the tungsten needle and the sample keeps the sample in position. For single fibers, the same method can be used, or if the fiber is longer (about 1 cm or more) it can be tightened so that only the ends of the fiber touch the sample cup. Special microsampling accessories of both types are available for commercial photoacoustic detectors. In microsamples, the moisture content in the photoacoustic cell has to be eliminated by using a desiccant to prevent water from dominating the weak photoacoustic signal of the microsample. Magnesium perchlorate is the most effective desiccant for water vapor [99].

Fig. 3.8 shows the effect described above. An 8 mm long hair fiber was measured both in the bottom of the sample cup and elevated by approximately 1.5 mm with a self-made sample holder. The ends of the fiber were clamped to the rim of the sample holder, while the rest of the fiber hung

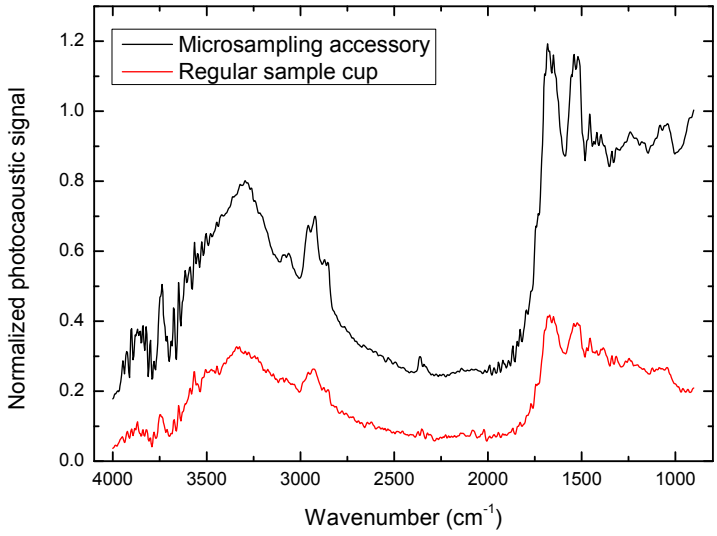

Figure 3.8: The same hair sample measured with an FTIR-PAS setup with and without microsampling accessory. The microsampling technique provided four times higher SNR.

freely. The Tensor 37 FTIR spectrometer and the PA301 photoacoustic detector were used in the measurements. In the measurement, 100 scans corresponding to 4 minutes of measurement time per sample, a 2.2 kHz scan velocity and 8 cm^{-1} resolution were used. A four-times higher SNR was achieved using this microsampling technique. In measurement times, it means a 16-fold measurement time to achieve the same SNR. Fig. 3.9 shows the measured spectra for even smaller hair samples. In this study, the smallest measured hair fiber had a length of 0.5 mm and an approximate diameter of 50 µm. Even with this small sample size, a spectrum with a sufficient SNR could be measured. A 5 mm single hair fiber should provide enough sample material for a detailed analysis using a cantilever-enhanced FTIR-PAS setup in most cases.

As previously mentioned, achieving sufficient reproducibility has been a problem in some of the earlier IR studies of single fibers with different methods. The same 5 mm hair sample was measured 10 times to investigate the repeatability of the measurement. The photoacoustic cell was opened and the sample was removed between each measurement. A standard de-

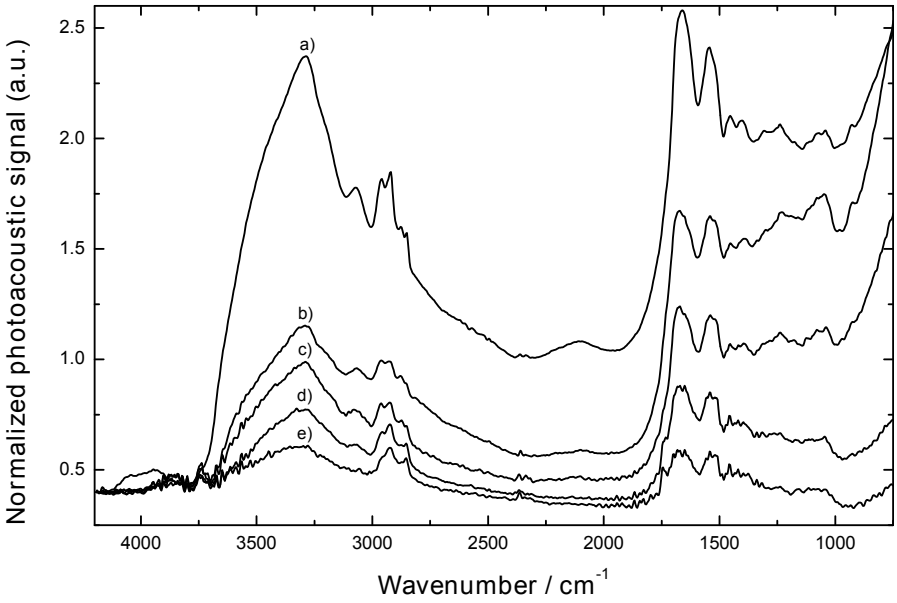

Figure 3.9: Photoacoustic spectra of hair samples of different sizes: a) a composition of hair fibers, b) 8 mm, c) 5 mm, d) 2 mm, and e) 0.5 mm piece of fiber. The spectrum of a) was divided with a factor of 3 for a better comparison. The offset of the spectra was corrected at 4200 cm^{-1}. [Paper V]

viation as low as 0.98 % in the amide I peak height was observed. Also, the heterogeneity of individual hair fibers from one person was investigated by measuring 10 different 5 mm long hair fibers. This time, the standard deviation in the amide I peak height was 4.59 %, which is still highly tolerable. The variation is a result of the slightly different compositions of the different hair fibers. The situation can be still improved by normalizing the peak intensities. As a conclusion, PAS shows a good repeatability of the measurement with hair microsamples. The performance is superior to, for example, an ATR sampling head.

3.3 Photoacoustic laser spectroscopy of solid samples

In the previous section, microsampling techniques were proposed to enhance the sensitivity of the photoacoustic detection. Another way to enhance the

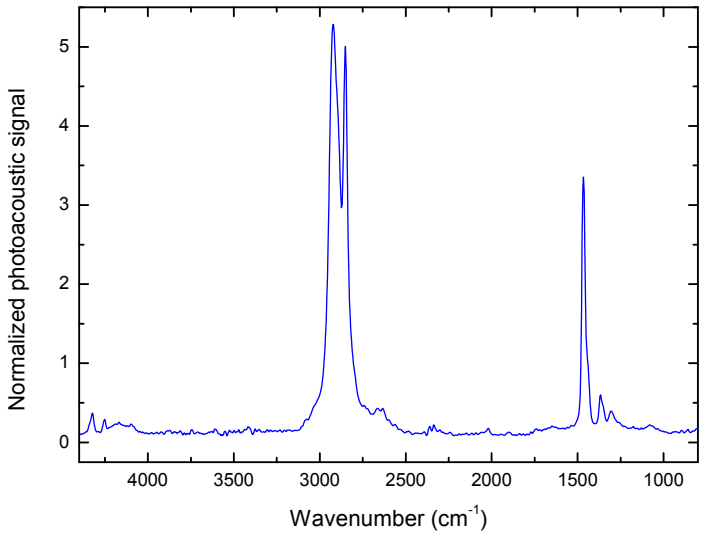

Figure 3.10: Mid-IR spectrum of a polyethylene disk measured with low resolution with FTIR-PAS.

sensitivity is to increase the source power. OPOs and EC-QCLs of today do also have sufficient tuning ranges for solid-phase applications. The use of an EC-QCL with solid samples was studied in Paper VI. In Fig. 3.10, a polyehylene ($(C_2H_4)_nH_2$) sample was measured with the Tensor 37 and PA301 FTIR-PAS setup with low resolution. The spectrum of polyethylene shows only a few features due to its simple structure. The mid-IR spectrum consists mainly of peaks of the CH_2 group, with minor features of the CH_3 group at the ends of the polymer chains. The same polyethylene sample was measured with FTIR and EC-QCL setups to investigate their high-resolution performance. A LaserTune (Block Engineering, Inc.) laser source was used with the PA301 in the EC-QCL measurement. The setup is illustrated in Fig. 2.5. The EC-QCL used had a tuning range of 676 cm^{-1} (970–1646 cm^{-1}), a line width of 1 cm^{-1}, and an average output power of a few mW. This broad tuning range of an EC-QCL has not been used in the photoacoustic spectroscopy of solids previously. The background was normalized with a carbon black sample and the intensities of the spectra were further normalized with respect to the CH_2 peak at 1460–1475 cm^{-1}.

The spectra for a polyethylene sample measured with both setups are

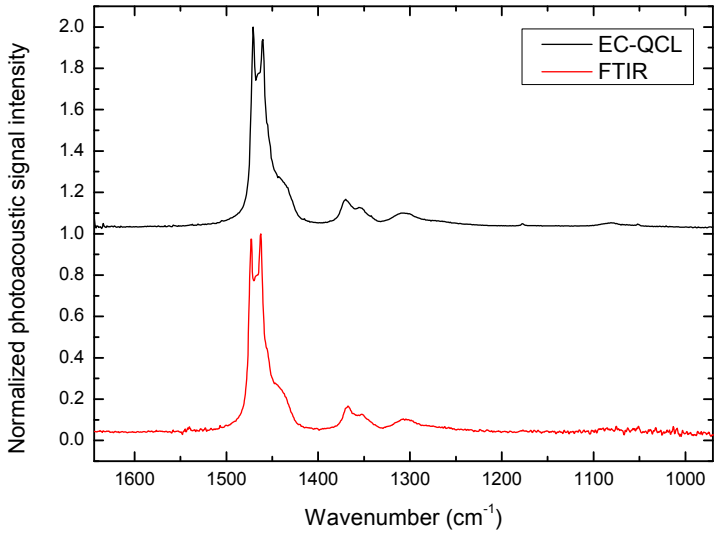

Figure 3.11: A mid-IR spectrum of a polyethylene disk measured with the EC-QCL and FTIR photoacoustic setups. The EC-QCL spectrum has an offset of 1 for a better visualization of the noise level. Both spectra share the same features as expected, but with a different SNR. [Paper VI]

shown in Fig. 3.11. The gain range of an EC-QCL cannot cover the full range of an FTIR instrument, so only the available tuning range is shown. The spectra show similar features, although the peak positions and relative intensities differ somewhat. The difference in the peak positions most probably relates to the tolerance in the wavelength accuracy of the EC-QCL, and the differences in the intensities are due to the sampling of the data points. Even with a 1 cm^{-1} resolution, the sharp peaks in the spectra are undersampled. Another difference is the noise. In this view, the EC-QCL spectrum appears virtually noiseless, while the FTIR spectrum shows clear noise, especially at wavenumbers below 1100 cm^{-1}. The SNR was calculated for the CH_2 peak at 1460–1475 cm^{-1} for both setups. The RMS noise was calculated from a straight and featureless part, between 1125 and 1155 cm^{-1}. The EC-QCL setup yielded roughly an order of magnitude better SNR.

The microsampling techniques of PAS can be combined with the high optical power and broad tunability of the EC-QCLs for sensitive high-

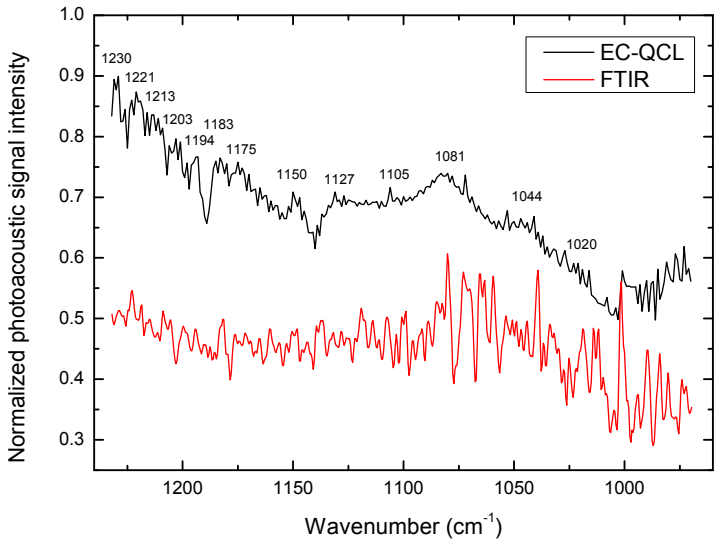

Figure 3.12: A single 8-mm hair fiber measured with high resolution using both EC-QCL and FTIR photoacoustic setups. The EC-QCL spectrum has an offset of 0.2 for a better visualization. The EC-QCL spectrum shows all the significant features of the hair sample in this wavenumber range, while the FTIR spectrum shows mainly noise. [Paper VI]

resolution spectroscopy of small samples. A single, 8 mm long hair fiber was measured with the EC-QCL PAS setup. Also, a comparative measurement of the same sample was made with the FTIR setup using the same measurement parameters. Fig. 3.12 shows the measured spectra for both cases. The performance of the EC-QCL setup is again superior to the FTIR setup. All the features in the spectrum of hair can be identified in the EC-QCL spectrum whereas the FTIR spectrum shows mainly noise. In small samples, the difference between the two setups is even larger, due to the considerably higher spectral radiance of the EC-QCL. Based on this result, the EC-QCL setup can be applied in situations where the conventional FTIR-PAS is unusable due to the lack of sensitivity.

In the conventional IR microspectroscopy, a synchrotron is applied as an IR source to be able to reach the smallest sample sizes. A synchrotron is a high-output source and is used to compensate the weak signals of small samples. The EC-QCL photoacoustic microspectroscopy method could be

a low-cost alternative for the use of a synchrotron. In addition to the lower price, such an EC-QCL photoacoustic devices could be built in a portable, even hand-held, size. Synchrotron IR microspectroscopy has many applications, for instance biological and biomedical applications, and is capable of measuring individual cells [97].

Chapter 4

Photoacoustic drug detection studies

4.1 Detection of drugs and drug precursors in the gas-phase

Screening cargo, as well as people and baggage, for illicit substances without impeding the throughput is a challenging task in customs, airports and harbors. While a false positive alarm can cost the industry time and money, a false negative alarm is a real security threat that can ultimately harm society [5, 7]. The inspection of individual cargo containers should also be performed within seconds rather than minutes [5, 100]. The optimal scenario would be to detect the precursors of the illicit substances even before the manufacturing of the actual drug has occurred. At present, there is no single superior technology for contraband detection [5]. Different detection schemes based on radiographic scanning, IMS and trained dogs have been proposed [5, 15, 100, 101]. In this study, CEPAS is applied in the gas-phase detection of cocaine and BMK.

4.1.1 Detection of cocaine

Cocaine (benzoylmethylecgonine, $C_{17}H_{21}NO_4$) in a powder form is a salt, typically cocaine hydrochloride [16]. Methyl benzoate (also benzoic acid and methyl ester, $C_6H_5CO_2CH_3$) is a product of the hydrolyzation of cocaine hydrochloride in moist air [5, 16, 101]. Cocaine hydrochloride exposed to any realistic humidity level in the environment produces methyl benzoate [102]. Drug-sniffing dogs are trained to detect the smell of methyl benzoate

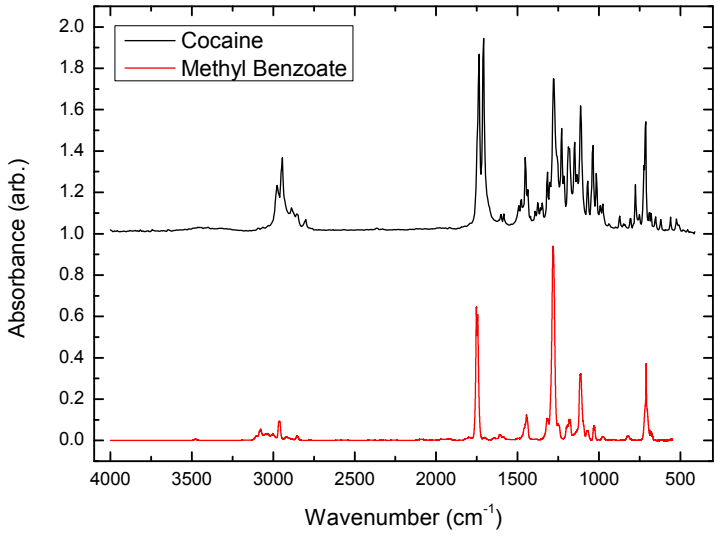

Figure 4.1: Mid-IR library spectra of pure cocaine and methyl benzoate. The spectrum of cocaine has an offset of 1 for a better visualization.

[101]. While methyl benzoate is the main hydrolysis product of cocaine hydrochloride, benzoylecgonine, methylecgonine and ecgonine are also formed [16, 103]. The IR spectra for cocaine and methyl benzoate are shown in Fig. 4.1. The spectrum of cocaine was taken from the Bruker drug library and the spectrum of methyl benzoate was from the PNNL database [104]. Both cocaine and methyl benzoate have a rich mid-IR spectrum, especially in the fingerprint region. Methyl benzoate was chosen for this study for its sharp, high-intensity peaks and because it is readily available from typical chemical suppliers.

Methyl benzoate was first studied with a broadly tunable EC-QCL PAS setup consisting of the LaserTune IR source and PA201 photoacoustic detector. The properties of the LaserTune were discussed in the previous chapter. Moving from left to right in Fig. 4.1, methyl benzoate has its strongest absorptions at 1718, 1272, 1109 and 675 cm^{-1}. Two of the highest intensity peaks (1272 and 1109 cm^{-1}) are found in the gain range of the used EC-QCL. Electrical 70 Hz amplitude modulation was used in the measurements and the laser was tuned in 1 cm^{-1} steps. A 10 ppm concentration of methyl benzoate in nitrogen was created by a Gasmet

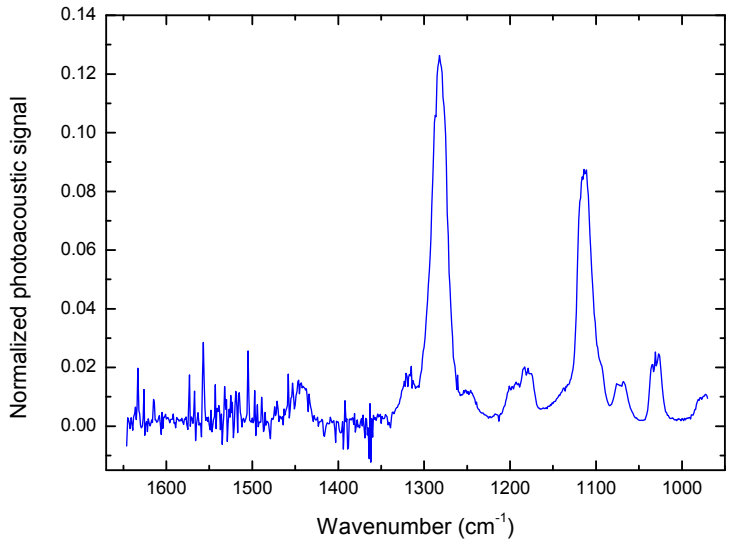

Figure 4.2: Vaporized methyl benzoate measured with the EC-QCL PAS setup using the broadly tunable LaserTune IR-source.

Calibrator (Gasmet Technologies, Inc.). A syringe containing methyl benzoate was mechanically depressed at a constant rate and vaporized at a constant temperature. The temperature was kept high enough to vaporize all the content from the tip of the needle immediately. The vaporized methyl benzoate was then guided into a nitrogen flow with a controlled rate produced with the use of mass flow meters. There was a one hour stabilization time before the measurements to the Gasmet Calibrator for stable conditions and operation. The measurements were performed at 950 mbar for uniform pressure conditions between different measurements.

A high quality, high-resolution photoacoustic spectrum measured with this setup is shown in Fig. 4.2. The measured spectrum was corrected with respect to the EC-QCL output power. The photoacoustic spectrum of methyl benzoate matches well with the PNNL library spectrum. The negative elements in the spectrum appear due to the removal of the spectrum of water and are pronounced because the laser output power is low in that region. Water was removed by first measuring a nitrogen background (with traces of water vapor) with similar conditions. Water peaks could be eliminated by a thorough purging of the beam path with nitrogen or

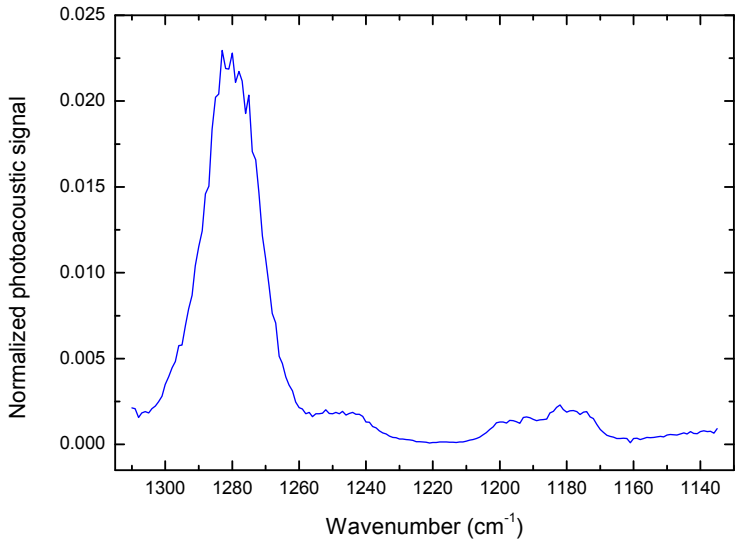

Figure 4.3: Vaporized methyl benzoate measured with the EC-QCL PAS setup using the Über Tuner IR-source.

similar non-IR active gas. However, in this study the main interest was to determine the performance of a broadly tunable EC-QCL in gas-phase photoacoustic detection and the water peaks appear as a natural part of this.

The performance of the photoacoustic method on methyl benzoate was further analyzed by using another EC-QCL with a narrower range of wavenumbers but with more output power. The output power of the LaserTune is low due to the broad tuning range. By using a narrower, but still more than sufficient, tuning range more output power can be targeted at the peaks of interest, and thus a lower detection limit can be achieved. Moreover, the tuning range is enough for performing actual spectroscopy or multi-component analysis. An Über Tuner (Daylight Solutions, Inc.) EC-QCL was used with the PA201. The range of the Über Tuner was 180 cm^{-1} (1130–1310 cm^{-1}), and was chosen to include the highest intensity peak (1280 cm^{-1}) of methyl benzoate. The measured photoacoustic spectrum for the full tuning range is shown in the Fig. 4.3. The output power of the EC-QCL also peaked near the highest intensity peak. The highest power of the Über Tuner was measured to be 18.5 mW, which is

Table 4.1: The achieved detection limit and the quantities used in the calculation of detection limit for methyl benzoate for the EC-QCL PAS setup.

Methyl benzoate signal (arb)	N_2 signal	N_2 RMS noise	LOD (0.9 s)
$4.79 \cdot 10^{-1}$	$3.13 \cdot 10^{-2}$	$5.08 \cdot 10^{-5}$	3.4 ppb

approximately an order of magnitude higher than that of the LaserTune. A rotating optical chopper with 70 Hz modulation frequency, 1 cm^{-1} tuning steps and 950 mbar pressure were used in the measurements.

The detection limit was calculated for the 1280 cm^{-1} peak. The noise of the system was quantified by calculating the RMS noise from the series of data points of the N_2 background signal while keeping the laser wavelength constant. A thorough overnight purging of the photoacoustic cell was conducted before the measurement of the nitrogen background spectrum and the time series was taken. Time series were collected for five different laser wavelengths. The measured time series of the N_2 signal at 1255 cm^{-1} is shown in Fig. 4.4. Like in the previous gas-phase experiment with formaldehyde, the signal has a form of a rising slope due to the water desorption from the cell walls. Therefore, a second order polynomial was fitted to the data to compensate for this effect. The rising slope was then removed from the data and the standard deviation for nine different regions of the data, each containing 20 data points, was calculated. The nine calculated standard deviations were then averaged for the final estimation of noise. However, in Fig. 4.4, data points 41–60 were removed from the calculation of the averaged standard deviation due to a visible disturbance in the measurement. Most probably, this disturbance is due to a mechanical vibration.

The quantities needed in the calculation of the detection limit are shown in Table 4.1. The detection limit of this setup for methyl benzoate for a 0.9 s measurement time (3 x RMS) was calculated to be 3.4 ppb. The detection limit for this measurement is low, which enables the use of this setup in real-life drug detection scenarios. For comparison, the detection limit for methyl benzoate for drug-trained dogs was reported to be 15 ppb [101]. However, in that study the dogs detected cocaine hydrochloride in lower concentrations, which indicates their sensitivity to other olfactory compounds. The methyl benzoate concentration due to hydrolysis from cocaine hydrochloride was determined by the same study to be about one

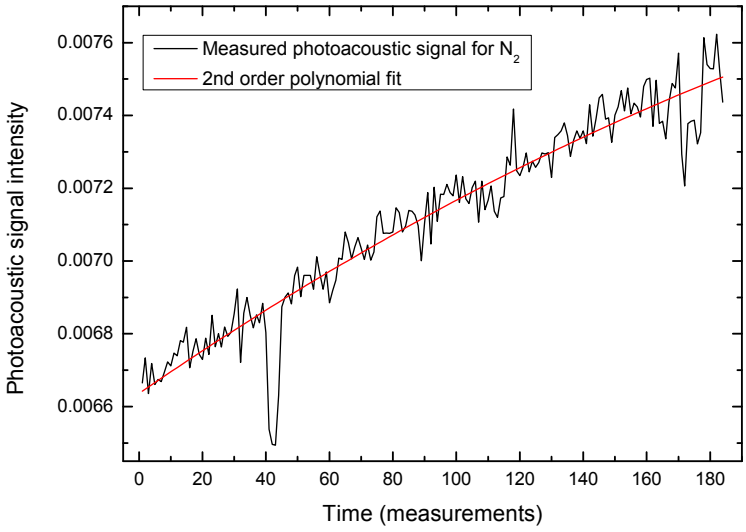

Figure 4.4: Time series of the photoacoustic signal of nitrogen and its second-order polynomial fit. The signal increase over time is due to desorption of water from the cell interior. Data points 40–45 show a disturbance in the measurement.

thousandth of the concentration due to the vaporization of pure methyl benzoate [101]. Although using trained dogs is a well-accepted technique for headspace drug detection, for example in airports and harbors, the sensitivity of such dogs depends on multiple factors, and the possible interfering compounds are nearly impossible to quantify.

4.1.2 Drug precursor measurements

The BMK ($C_6H_5CH_2C(O)CH_3$) compound is a drug precursor that is used to manufacture amphetamine and methamphetamine. Methyl benzyl ketone, phenylacetone and phenyl-2-propanone (P2P) can also be used equivalently for that chemical formula. BMK is the main starting material in the production of methamphetamine, and thus a controlled substance by the Drug Enforcement Administration of the U.S. Department of Justice [105]. A secure source of BMK is needed for methamphetamine production, which has led some unlawful chemists to produce their own. The end

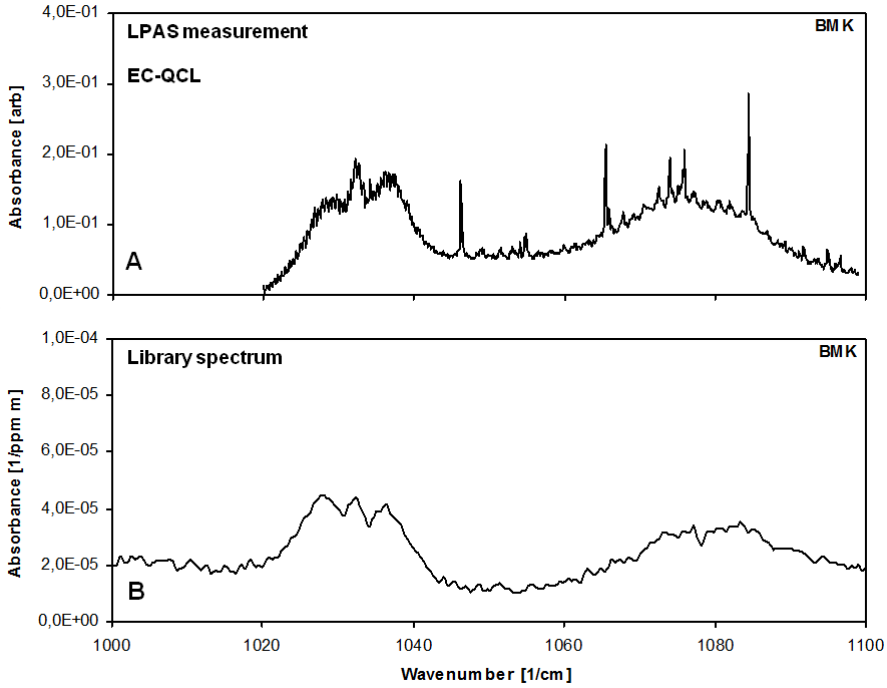

Figure 4.5: *Upper graph:* Photoacoustic spectrum of BMK measured with the EC-QCL PAS setup. *Lower graph:* Library FTIR spectrum of BMK. [Paper I]

product is then applied for own use, or for sale. BMK can be synthesized in a number of different ways, but precursors of BMK are also controlled substances [16, 105].

BMK was measured with an EC-QCL PAS setup consisting of TLS-21095-MHF (Daylight Solutions, Inc.) CW EC-QCL and the PA201. The arrangement of the setup was similar to Fig. 3.1, although Gasmet Calibrator was used for the generation of the gas-phase BMK sample. The maximum output of the CW EC-QCL was 64.5 mW and the full tuning range was 80 cm^{-1} (1020–1100 cm^{-1}). A rotating optical chopper with a 61 Hz modulation frequency was used in this measurement. A 48 ppm BMK sample in a nitrogen flow was created with the Gasmet Calibrator. The measured photoacoustic spectrum and a library spectrum for BMK are shown in Fig. 4.5. The sharp peaks in the spectrum are ammonia residuals and the periodic behavior is due to the laser power variation at different wavenumbers. The detection limit was calculated in the same manner as for formaldehyde and methyl benzoate previously. The detection limit was

calculated for the 1032 cm^{-1} peak. The laser output power at that point was 34 mW. The calculated detection limit (3 x RMS noise level) for 0.9 s measurement time was 26 ppb. The parameters used in the calculation are shown in Paper I.

This result could be considerably improved by measuring a higher intensity peak in the spectrum of BMK. However, the peak at 1032 cm^{-1} was the strongest absorption feature in the gain range of the EC-QCL used in this study. With this result, the identification of BMK from trace elements in the air within a short time scale can already be considered realistic. The calculated vapor concentration from the vapor pressure of BMK at room temperature is 300 ppm, which is more than two orders of magnitude higher than the calculated detection limit. Furthermore, in Paper I it was estimated that for the 1222 cm^{-1} peak and 100 mW laser output power, the detection limit for 1 s measurement time is 2.0 ppb. This estimation was based on the selected optimal tuning range of 1080–1280 cm^{-1} from that study. However, this is not yet the optimal case for BMK, as a 1750 cm^{-1} peak yields a signal approximately three times higher than the 1222 cm^{-1} peak based on an FTIR measurement. Estimations for other drug precursors, acetic anhydride (heroin), ephedrine (amphetamine) and safrole (ecstasy), were also made based on the FTIR measurements. The calculated estimations were in the low- or sub-ppb range. The proposed improvements can be applied and the 200 cm^{-1} tuning range is sufficient for the multi-component analysis of these four compounds.

4.1.3 Summary

Drug and drug precursor studies have yielded low ppb-level detection limits, which are sufficient for practical applications in headspace detection. The detection limits can be further lowered by the use of higher output laser sources or solid-phase microextraction, which is a common practice in IMS, for example. However, the ultimate sensitivity of the system is determined by the number of possible interfering compounds. Determining the cross-interference of different compounds requires the addition of spectral analysis methods. Spectral analysis based on spectral libraries can be a powerful tool, which is adaptive to different backgrounds and to adding new components. This method could also be applied to the detection of toxic vapors, chemical warfare agents (CWA), or hidden persons, among other applications. Indeed, PAS is already an established technique in the field of CWAs [6].

4.2 Detection of cocaine abuse in hair

Cocaine is difficult to detect through observations alone and blood or urine tests are usually performed for certainty [16]. Hair testing for cocaine has been evaluated as a routine practice in forensic toxicological laboratories [32, 33, 35]. Hair offers an alternative or complementary matrix, and hairs are routinely collected during criminal investigations [33]. Two different approaches in the detection of cocaine traces in hair were applied in this study: rapid-scan FTIR-PAS measurement combined with principal component analysis (PCA) and step-scan FTIR-PAS.

4.2.1 Photoacoustic measurement combined with statistical analysis

Hair samples from 12 cocaine-overdose patients were measured with the FTIR-PAS setup, consisting of the Tensor 37 and the PA301. The subjects were frequent users, which implies that cocaine should be found from the full length of the hairs. The drug content in the hair samples was measured previously with GC/MS. The drug content varied from 1.5 to 38 ng/mg between different patients. For each photoacoustic measurement, 20–30 mg of hair material was used. A similar-sized group of drug-free hair samples was also measured as a reference. The idea of the study was to discriminate the drug containing samples from the reference samples, without any separation or extraction procedures, with a simple FTIR-PAS measurement and PCA. More details of this study can be found in Paper IV.

In Fig. 4.6, the average spectra for drug-containing hair samples and reference samples along with a library spectrum of pure cocaine, are shown. When we investigate Fig. 4.6, no discrimination can be made based on the averaged spectra. This is due to the small concentrations of cocaine in the hair and overlapping spectral features. Clearly, this situation is the same when investigating the individual spectra. Therefore, statistical methods are needed to distinguish between the drug users and the reference group. However, statistical methods alone are not enough to solve the problem, and data pre-processing is needed. In Fig. 4.7, PCA is applied to the measured spectra without any spectral processing. The individual hair samples are rather randomly organized, and no discrimination can be made based on these results. Although only principal components (PC) 1 and 2 are shown, the discrimination does not improve even if different combinations of higher PCs are used. Therefore, applying PCA directly to the dataset is not

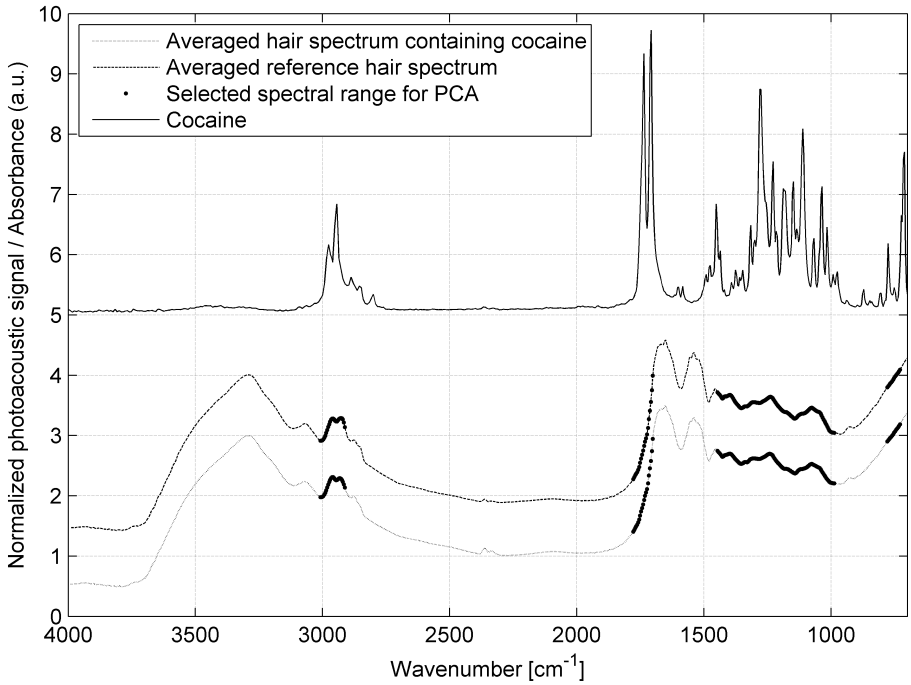

Figure 4.6: Top: Pure cocaine spectrum (from the Bruker drug library). Bottom: Average of measured hair spectra for both cocaine-containing and non-cocaine-containing hair samples with the spectral filter for data analysis. For better visibility, the cocaine spectrum is multiplied by 5 and plotted with an offset of 4. [Paper IV]

sufficient.

Spectral pre-processing

Spectral pre-processing was needed for extracting the cocaine-related information in hair. First, the optimal spectral range for the PCA had to be selected. The logical starting point is to choose the regions in which cocaine has absorption. However, this appears not to be the optimal choice, as there is interference between cocaine and the sample matrix: in this case, hair keratin. For example, the highest intensity peak of cocaine, which is the C=O bond around 1750 cm^{-1}, interferes with a much stronger amide I peak in hair. The intensity of the amide I peak in the spectrum of hair varies greatly between different individuals. However, the C=O peak is the most important single feature in the spectrum of cocaine, and cannot

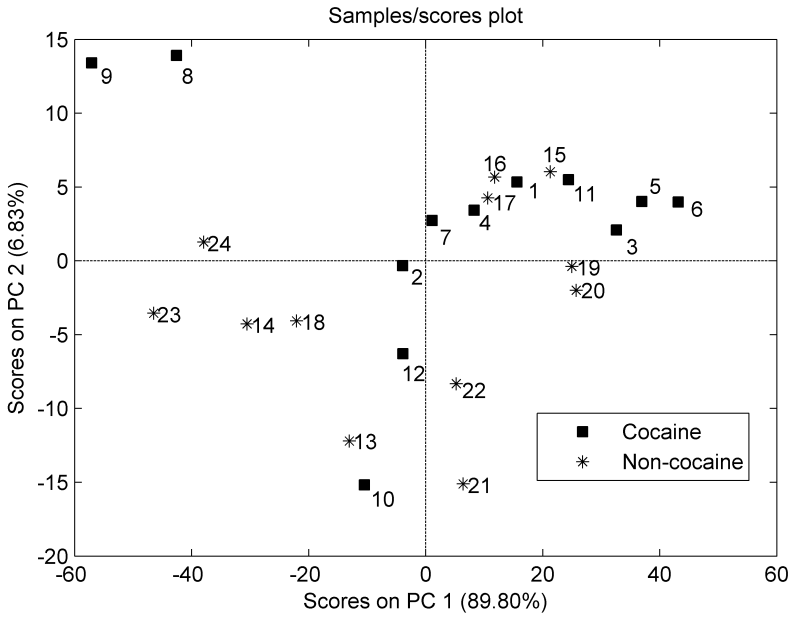

Figure 4.7: Scores plot of PC1 and PC2 without the pre-processing. The percentages on the axis titles relate to the amount of explained variance in the PCA. The samples in the plot do not divide into groups, and the discrimination of cocaine users cannot be done. [Paper IV]

be entirely ignored. Therefore, choosing the optimal spectral range was investigated thoroughly. The selected spectral range is shown in Fig. 4.6. Second, the intensity of the photoacoustic signal varied notably between the different samples. Therefore, the spectra had to be normalized. Normalization was performed by dividing each variable (spectral point) of the PCA by the sum of all variables. In other words, the spectra were normalized to their area. Third, the spectra had to be derived for a more pronounced lineshape. The second derivative was chosen as being the most suitable for this study. Last, because the dataset was mean centered, the intensity of each spectral point was divided by the mean of intensities at that point to balance the different variables. This pre-processing is discussed in detail in Paper IV.

Results and classification

After the pre-processing described above, PCA was performed with the data. Fig. 4.8 shows the PC1 and PC2 for the calculated PCA model

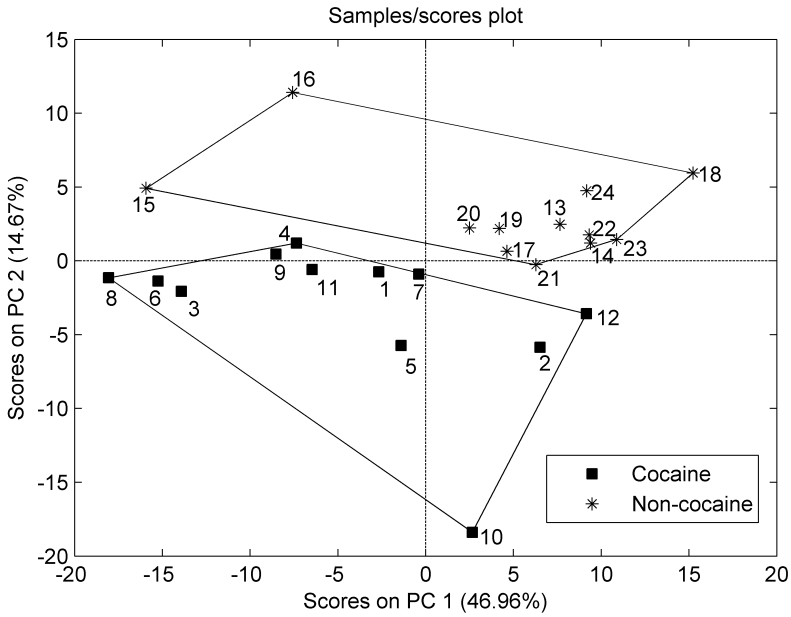

Figure 4.8: Scores plot of PC1 and PC2 with the pre-processing methods developed in this study. In this plot, the samples divide into two groups according to cocaine content and cocaine users can be discriminated. [Paper IV]

with the pre-processing. This time, the samples divided into two groups according to their cocaine content. The hair samples can be discriminated according to their cocaine content, although the distance between the two classes in the PC1–PC2 space is narrow. While 10 PCs were calculated, higher PCs did not give any better discrimination. The explained variance is 46.96 % for PC1 and 14.67 % for PC2. Although PC2 has about a third of the explained variance, it still contributes at least as much as PC1 to the classification. Therefore, all the explained variance does not come solely from the cocaine content, meaning that there are other factors interfering in the separation. The sources for additional variance include the natural variation between different individuals, and chemical exposure and weathering of the hair fibers. The method worked acceptably, although the separation could be improved. The key to successful discrimination was the spectral pre-processing. Although the method succeeded in discriminating the cocaine-containing hair samples, the method is not yet robust enough to be used to confirm the use of cocaine in drug testing. To make a more general model, more samples are needed.

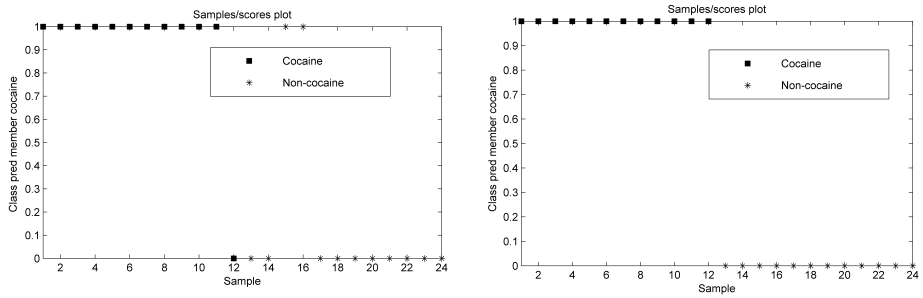

(a) **(b)**

Figure 4.9: Classification methods for PCA. Samples 1–12 contain cocaine and 13–24 do not contain cocaine. a) Prediction of the KNN model: all samples, with the exception of samples 12, 15, and 16, were predicted correctly. b) Prediction of the SVM model: all samples were predicted correctly.

Two different classification methods–k-nearest neighbors (KNN) and support vector machines (SVM)–were used in the verification of the results. The same data set with the same pre-processing was used. Since a data set of 24 hair samples is rather small, no separate test set was used. The SVM method predicted all of the samples correctly, while KNN predicted 3 samples incorrectly. These samples can be identified as the ones at the edges of the selected boundaries (samples 2, 15 and 16 in Fig. 4.8). The results of the classification methods are shown in Fig. 4.9. The KNN and the SVM results are in compliance with the PCA results.

4.2.2 Measurement of the carbonyl group of cocaine

Cocaine detection in hair with rapid-scan FTIR-PAS suffers from short thermal diffusion lengths due to the high modulation frequencies. For optimal conditions, a deeper penetration in the sample is needed as the cocaine is mainly concentrated in the medulla of the hair [27]. Therefore, step-scan FTIR-PAS measurements were performed to obtain a longer thermal diffusion length. The measurements were performed with the same data set as the previous study. The spectra were recorded with an FTS6000 (Bio-Rad Laboratories, Inc.) FTIR spectrometer, capable of step-scan, and the PA301. A 100 Hz scan velocity was used in the measurements. When compared to the minimum scan velocity of 2.2 kHz in Tensor 37, a 100 Hz scan velocity gives a 4.7 times longer thermal diffusion length, according to Eq. 2.3.

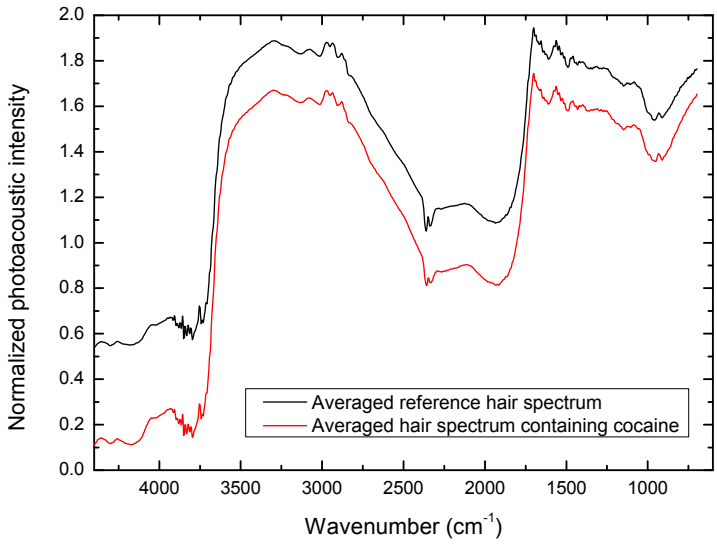

Figure 4.10: Average of measured step-scan FTIR-PAS hair spectra for both cocaine-containing and non-cocaine-containing hair samples.

Fig. 4.10 shows the averaged step-scan FTIR-PAS spectra for the cocaine hair samples and the reference group. The spectra look different when compared to Fig. 4.6 due to the different resonance conditions of substantially lower modulation frequencies. Although a longer thermal diffusion length is obtained, the spectra are notably more saturated due to the lower modulation frequencies, which complicates the analysis. The features in the spectra are compressed, which can be especially seen in the fingerprint region. Due to the saturation, the water vapor content interferes strongly with the actual spectral features of the sample, although the spectrometer was purged with nitrogen constantly and the photoacoustic cell was purged with helium between the measurements. The effect of water vapor can be seen in the amide I and II bands in Fig. 4.10, where a sharp and fragmentary bandshape is observed instead of the smooth shape found in Fig. 4.6. Due to the saturation, the natural variances, and for example a differing baseline, are also more pronounced. In this case, PCA mainly observed the differences in the sample matrix and in the measurement instead of the cocaine content, and cannot be applied in the discrimination.

Although PCA appeared to be useless in these measurements, useful

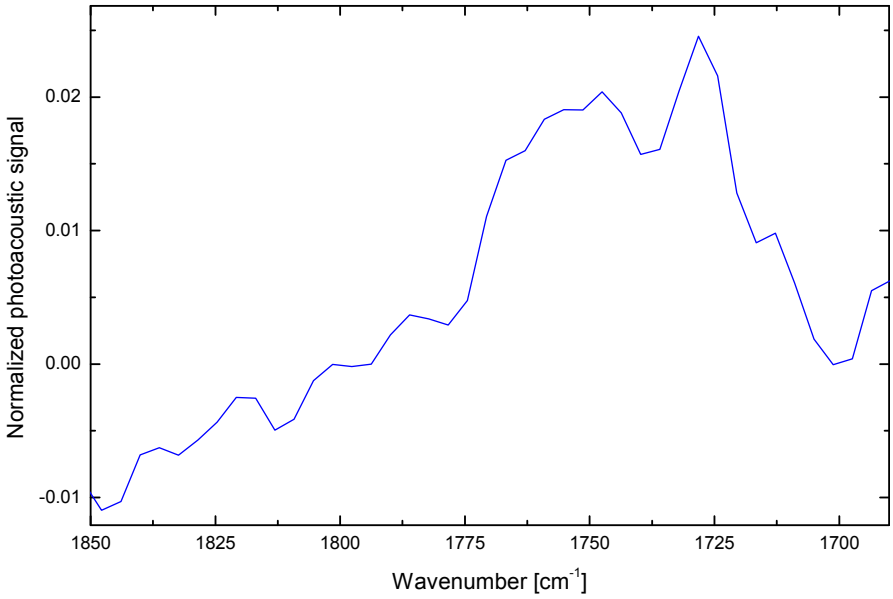

Figure 4.11: The C=O double peak of the carbonyl group of cocaine in hair. Photoacoustic mean spectrum of the reference hair samples was subtracted from the mean spectrum of the drug hair samples. As a result, the C=O bond of cocaine can be distinguished in the difference spectrum.

data was gained. The most prominent feature in the spectrum of cocaine, the C=O vibration of the carbonyl group, could be resolved in the difference spectrum of the averaged spectrum of the cocaine sample group and the averaged spectrum of the reference group. The resolved C=O peak is shown in Fig. 4.11. The C=O peak was not resolved directly from the individual spectra, because it interfered with a much stronger amide I peak, as previously stated. Furthermore, the peak was not resolved in the difference spectrum of individual spectra due to a high variance in the sample matrix. However, it was distinguished in the averaged spectra as the differences in the sample matrix even out with the averaging. A more thorough data pre-processing should be applied to the spectra for better results.

4.2.3 Summary

The results presented in this section prove that drug detection in hair without any separation or extraction procedures and sample preparation

is possible with cantilever-enhanced FTIR-PAS. However, neither of the proposed methods is yet optimal. The photoacoustic method for drug detection in hair could be improved with the use of the techniques introduced in Chapter 3. The use of EC-QCL enables high-SNR, high-resolution studies of single hair fibers. Moreover, contrary to an FTIR instrument with a continuous scan, the use of an external modulation provides a controlled sampling depth. Drug detection with single fibers brings the method closer to practical use.

Chapter 5

Conclusions

This study concerned several approaches to different drug-detection schemes with CEPAS. Different techniques were combined to achieve an ultimate sensitivity. Successful results were obtained from both gas- and solid-phase measurements. Low- or sub-ppb-level detection limits were obtained for formaldehyde, methyl benzoate, and BMK with different LPAS setups. Cocaine overdose patients were discriminated from a reference group by the cocaine content in hair with an FTIR-PAS setup combined with PCA and sufficient data pre-processing. In addition, solid-phase LPAS and the microsampling techniques of PAS were investigated.

The CEPAS method was shown to have several advantages in this study. A high sensitivity was obtained in both laser and FTIR applications. The use of QCLs enabled the low detection limits in gas-phase studies. EC-QCLs broadened not only the available tuning ranges, but also the scope of possible applications by enabling solid-phase studies. The single most interesting thing in CEPAS at this time is the EC-QCL. The rapid evolution of EC-QCLs has enabled the practical use of lasers, which can now also be constructed in a small size. Photoacoustic spectrometers with EC-QCLs can now be built to be simultaneously selective, sensitive, fast and compact.

Combining all the techniques used in this study into a prototype designed for a specific application would be a logical step in the future. The decision between gas- or solid-phase measurements defines the design and the possible applications. However, in each case the high optical power and broad tuning range of the EC-QCLs would be combined to a cantilever-enhanced photoacoustic cell optimized for small samples. The result would be a hand-held photoacoustic IR spectrometer with a high resolution and spectral density, and ultimate sensitivity.

Drug detection was an example of one possible application of this method,

but it can easily be transferred to other uses. It would probably also be possible to even cover several different applications with a single setup. The possible applications in the gas-phase for such a prototype would include the detection of toxic substances, CWAs, explosives or hidden persons. For a solid-phase prototype, the possible applications would include disease diagnostics using hair, skin or another matrix, the material identification of licit and illicit drugs, and textile fiber analysis for forensic studies.

Bibliography

[1] J. Kottmann, J. M. Rey, J. Luginbühl, E. Reichmann, and M. W. Sigrist, Biomedical Optics Express **3**, 667 (2012).

[2] K. M.-C. Hans, S. Müller, and M. W. Sigrist, Drug Testing and Analysis **4**, 420 (2012).

[3] P. Kintz and P. Mangin, Forensic Science International **73**, 93 (1995).

[4] V. A. Boumba, K. S. Ziavrou, and T. Vougiouklakis, International Journal of Toxicology **25**, 143 (2006).

[5] H. Lai, I. Corbin, and J. R. Almirall, Analytical and Bioanalytical Chemistry **392**, 105 (2008).

[6] R. Sferopoulos, *A Review of Chemical Warfare Agent (CWA) Detector Technologies and Commercial-Off-The-Shelf Items* (Human Protection and Performance Division, Australia, 2009).

[7] UNODC, *World Drug Report 2013* (United Nations publication, Sales No. E.13.XI.6, 2013).

[8] K. H. Michaelian, *Photoacoustic infrared spectroscopy*, 1st ed. (John Wiley & Sons, Inc., 2003).

[9] C. Haisch, Measurement Science and Technology **23**, 012001 (2012).

[10] J. Kauppinen, K. Wilcken, I. Kauppinen, and V. Koskinen, Microchemical Journal **76**, 151 (2004).

[11] T. Kuusela and J. Kauppinen, Applied Spectroscopy Reviews **44**, 443 (2007).

[12] R. E. Lindley, A. M. Parkes, K. A. Keen, E. D. McNaghten, and A. J. Orr-Ewing, Applied Physics B **86**, 707 (2007).

[13] R. F. Curl, F. Capasso, C. Gmachl, A. A. Kosterev, B. McManus, R. Lewicki, M. Pusharsky, G. Wysocki, and F. K. Tittel, Chemical Physics Letters **487**, 1 (2010).

[14] A. Hugi, R. Maulini, and J. Faist, Semiconductor Science and Technology **25**, 083001 (2010).

[15] J. E. Parmeter, D. W. Murray, and D. W. Hannum, *Guide for the Selection of Drug Detectors for Law Enforcement Applications* (National Institute of Justice, Office of Science and Technology, Washington, 2000).

[16] F. P. Smith, *Forensic Drug Analysis*, 1st ed. (Elsevier, Inc., 2005).

[17] R. Bartlome, J. M. Rey, and M. W. Sigrist, Analytical Chemistry **80**, 5334 (2008).

[18] S. Mengali, N. Liberatore, D. Luciani, R. Viola, G. C. Cardinali, I. Elmi, A. Poggi, S. Zampolli, E. Biavardi, E. Dalcanale, F. Bonadio, O. Delemont, P. Esseiva, and F. S. Romolo, Proc. of SPIE **8631**, 86312F1 (2013).

[19] E. G. Bartick, "Infrared and raman spectroscopy in forensic science," (John Wiley & Sons, Inc., 2012) Chap. Criminal Forensic Analysis, pp. 89–109, 1st ed.

[20] "European Commission FP7 project CUSTOM," http://www.custom-project.eu, accessed 31.10.2013.

[21] "European Commission FP7 project DOGGIES," http://www.fp7-doggies.eu, accessed 31.10.2013.

[22] M. D. Hargreaves, "Infrared and raman spectroscopy in forensic science," (John Wiley & Sons, Inc., 2012) Chap. Drugs of Abuse - Application of Handheld FT-IR and Raman Spectrometers, pp. 339–349, 1st ed.

[23] K. M.-C. Hans, M. Müller, T. Petrosyan, and M. W. Sigrist, Analytical Methods (2013).

[24] K. M.-C. Hans, M. Müller, M. Gianella, P. Wägli, and M. W. Sigrist, Proc. SPIE **8591**, 85910F (2013).

[25] Y.-C. Chang, P. Wägli, V. Paeder, A. Homsy, L. Hvozdara, P. van der Wal, J. Di Francesco, N. F. de Rooij, and H. P. Herzig, Lab Chip **12**, 3020 (2012).

[26] P. Wägli, Y.-C. Chang, A. Homsy, L. Hvozdara, H. P. Herzig, and N. F. de Rooij, Analytical Chemistry **85**, 7558 (2013).

[27] K. S. Kalasinsky, Cellular and Molecular Biology **44**, 81 (1998).

[28] K. S. Kalasinsky, J. Magluilo Jr., and T. Schaefer, Forensic Science International **63**, 253 (1993).

[29] A. M. Baumgartner, P. F. Jones, W. A. Baumgartner, and C. T. Black, The Journal of Nuclear Medicine **20**, 748 (1979).

[30] C. R. Robbins, *Chemical and Physical Behavior of Human Hair*, 4th ed. (Springer-Verlag New York, Inc., 2002).

[31] P. Kintz, *Drug Testing in Hair*, 1st ed. (CRC Press, Inc., 1996).

[32] P. Kintz, *Analytical and Practical Aspects of Drug Testing in Hair*, 1st ed. (CRC Press, Inc., 2007).

[33] G. A. Cooper, R. Kronstrand, and P. Kintz, Forensic Science International **218**, 20 (2012).

[34] F. Musshoff and B. Madea, Forensic Science International **165**, 204 (2007).

[35] C. Stramesi, C. Vignali, A. Groppi, M. Caligara, F. Lodi, S. Pichini, and C. Jurado, Forensic Science International **218**, 101 (2012).

[36] A. G. Bell, American Journal of Science **20**, 305 (1880).

[37] A. Rosencwaig, Annual Review of Biophysics and Bioengineering **9**, 31 (1980).

[38] C. Haisch and R. Niessner, Spectroscopy Europe **14**, 10 (2002).

[39] A. Rosencwaig and A. Gersho, Journal of Applied Physics **47**, 64 (1976).

[40] F. A. McDonald and G. C. Wetsel Jr., Journal of Applied Physics **49**, 2313 (1978).

[41] L. Aamodt, J. Murphy, and J. Parker, Journal of Applied Physics **48**, 927 (1977).

[42] J. F. McClelland, R. W. Jones, and S. J. Bajic, "Handbook of vibrational spectroscopy," (John Wiley & Sons, Ltd., 2002) Chap. FT-IR Photoacoustic Spectroscopy.

[43] J. Kottmann, J. M. Rey, and M. W. Sigrist, Review of Scientific Instruments **82**, 084903 (2011).

[44] K. Wilcken and J. Kauppinen, Applied Spectroscopy **57**, 1087 (2003).

[45] V. Koskinen, J. Fonsen, J. Kauppinen, and I. Kauppinen, Vibrational Spectroscopy **42**, 239 (2006).

[46] V. Spagnolo, A. A. Kosterev, L. Dong, R. Lewicki, and F. K. Tittel, Applied Physics B **100**, 125 (2010).

[47] A. Kosterev, G. Wysocki, Y. Bakhirkin, S. So, R. Lewicki, M. Fraser, F. Tittel, and R. F. Curl, Applied Physics B **90**, 165 (2008).

[48] M. J. D. Low and G. A. Parodi, Spectroscopy Letters **13**, 663 (1980).

[49] S. M. Riseman and E. M. Eyring, Spectroscopy Letters **14**, 163 (1981).

[50] C. H. Lochmüller, R. Röhl, and D. B. Marshall, Analytical letters **14**, 41 (1981).

[51] M. J. D. Low, Spectroscopy Letters **16**, 913 (1983).

[52] R. W. Jones and J. F. McClelland, Applied Spectroscopy **55**, 1360 (2001).

[53] Y. C. Teng and B. S. H. Royce, Applied Optics **21**, 77 (1982).

[54] R. O. Carter III and M. C. Paputa Peck, Applied Spectroscopy **43**, 468 (1989).

[55] R. O. Carter III and S. L. Wright, Applied Spectroscopy **45**, 1101 (1991).

[56] S. J. McGovern, B. S. H. Royce, and J. B. Benziger, Journal of Applied Physics **57**, 1710 (1985).

[57] D. J. Lyman and P. Schofield, Applied Spectroscopy **62**, 525 (2008).

[58] S. Ekgasit and H. Ishida, Vibrational Spectroscopy **13**, 1 (1996).

[59] F. Fondeur and B. S. Mitchell, Spectrochimica Acta Part A **56**, 467 (2000).

[60] N. A. Freebody, A. S. Vaughan, and A. M. Macdonald, Analytical and Bioanalytical Chemistry **396**, 2813 (2010).

[61] M. Halttunen, J. Tenhunen, T. Saarinen, and P. Stenius, Vibrational Spectroscopy **19**, 261 (1999).

[62] C. Q. Yang, Applied Spectroscopy **45**, 102 (1991).

[63] A. A. Kosterev, Y. A. Bakhirkin, R. F. Curl, and F. K. Tittel, Optics Letters **27**, 1902 (2002).

[64] V. Saptari, *Fourier-Transform Spectroscopy Instrumentation Engineering*, 1st ed. (SPIE Press, Ltd., 2003).

[65] P. R. Griffiths and J. A. de Haseth, *Fourier transform infrared spectrometry*, 2nd ed. (John Wiley & Sons, Inc., 2007).

[66] J. Kauppinen and J. Partanen, *Fourier Transforms in Spectroscopy*, 1st ed. (Wiley-VCH Verlag Berlin GmbH, 2001).

[67] M. J. Adams, *Chemometrics in Analytical Spectroscopy*, 1st ed. (The Royal Society of Chemistry, 1995).

[68] Q. Wen and K. H. Michaelian, Optics Letters **33**, 1875 (2008).

[69] K. H. Michaelian and Q. Wen, Journal of Physics: Conference Series **214**, 012004 (2010).

[70] E. L. Holthoff, L. S. Marcus, and P. M. Pellegrino, Applied Spectroscopy **66**, 987 (2012).

[71] J. Coates, BioPhotonics **17**, 1 (2010).

[72] T. Salthammer, S. Mentese, and R. Marutzky, Chemical Reviews **110**, 2536 (2010).

[73] L. S. Rothman, I. E. Gordon, A. Barbe, D. C. Benner, P. F. Bernath, M. Birk, V. Boudon, L. R. Brown, A. Campargue, J.-P. Champion, K. Chance, L. H. Coudert, V. Dana, V. M. Devi, S. Fally, J.-M. Flaud, R. R. Gamache, A. Goldman, D. Jacquemart, I. Kleiner, N. Lacome, W. J. Lafferty, J.-Y. Mandin, S. T. Massie, S. N. Mikhailenko, C. E. Miller, N. Moazzen-Ahmadi, O. V. Naumenko, A. V. Nikitin, J. Orphal, V. I. Perevalov, A. Perrin, A. Predoi-Cross, C. P. Rinsland, M. Rotger, M. Šimečková, M. A. H. Smith, K. Sung, S. A. Tashkun, J. Tennyson, R. A. Toth, A. C. Vandaele, and J. Vander Auwera, Journal of Quantitative Spectroscopy & Radiative Transfer **110**, 533 (2009).

[74] "Finnish Institute of Occupational Health: formaldehyde: effects to health and exposure," http://www.ttl.fi/fi/kemikaaliturvallisuus/ainekohtaista_kemikaalitietoa/formaldehydi/formaldehydin_terveysahaitat_ja_ltistuminen/ sivut/default.aspx, accessed 31.10.2013.

[75] L. E. Jurdana, K. P. Ghiggino, I. H. Leaver, C. G. Barraclough, and P. Cole-Clarke, Applied Spectroscopy **48**, 44 (1994).

[76] E. Y. Jiang, Applied Spectroscopy **53**, 583 (1999).

[77] L. E. Jurdana, K. P. Ghiggino, I. H. Leaver, and P. Cole-Clarke, Applied Spectroscopy **49**, 361 (1995).

[78] T. Watanabe, A. Tamura, Y. Yoshimura, and H. Nakazawa, Analytical Biochemistry **254**, 267 (1997).

[79] D. J. Lyman and J. Murray-Wijelath, Applied Spectroscopy **59**, 26 (2005).

[80] V. Signori and D. M. Lewis, International Journal of Cosmetic Science **19**, 1 (1997).

[81] J. Strassburger and M. M. Breuer, Journal of the Society of Cosmetic Chemists **36**, 61 (1985).

[82] J.-L. Bantignies, G. L. Carr, D. Lutz, S. Marull, G. P. Williams, and G. Fuchs, Journal of Cosmetic Science **51**, 73 (2000).

[83] C. R. Robbins and C. H. Kelly, Textile Research Journal **40**, 891 (1970).

[84] N. H. Leon, Journal of the Society of Cosmetic Chemistist **23**, 427 (1972).

[85] J. Kong and S. Yu, Acta Biochimica et Biophysica Sinica **39**, 549 (2007).

[86] V. P. Gupta and T. A. Keiderling, Biopolymers **32**, 239 (1992).

[87] A. Barth and C. Zscherp, Quarterly Reviews of Biophysics **35**, 369 (2002).

[88] Z. Movasaghi, S. Rehman, and I. ur Rehman, Applied Spectroscopy Reviews **43**, 134 (2008).

[89] W.-S. Lee, Journal of Dermatological Science **64**, 153 (2011).

[90] S. Cai and B. R. Singh, Biochemistry **43**, 2541 (2004).

[91] S. Y. Venyaminov and N. N. Kalnin, Biopolymers **30**, 1243 (1990).

[92] K. Rahmelow, W. Hübner, and T. Ackermann, Analytical Biochemistry **257**, 1 (1998).

[93] J. Hopkins, L. Brenner, and C. S. Tumosa, Forensic Science International **50**, 61 (1991).

[94] L. Farren, S. Shayler, and A. R. Ennos, The Journal of Experimental Biology **207**, 735 (2004).

[95] R. G. Schipper, E. Silletti, and M. H. Vingerhoeds, Archives of Oral Biology **52**, 1114 (2007).

[96] C. P. Schultz, M. K. Ahmed, C. Dawes, and H. H. Mantsch, Analytical Biochemistry **240**, 7 (1996).

[97] P. Dumas and L. Miller, Vibrational Spectroscopy **32**, 3 (2003).

[98] M. Gniadecka, O. F. Nielsen, D. H. Christensen, and H. C. Wulf, The Journal of Investigative Dermatology **110**, 393 (1998).

[99] *Multisampler Instructions*, MTEC Photoacoustics, Inc. (1997).

[100] V. J. Orphan, E. Muenchau, J. Gormley, and R. Richardson, Applied Radiation and Isotopes **63**, 723 (2005).

[101] L. P. Waggoner, J. M. Johnston, M. Williams, and J. Jackson, Proc. of SPIE **2937**, 216 (1997).

[102] L. E. Dejarme, R. E. Gooding, S. J. Lawhon, P. Ray, and M. R. Kuhlman, Proc. of SPIE **2937**, 19 (1997).

[103] K. G. Furton, Y.-c. Hong, Y.-L. Hsu, T. Luo, S. Rose, and J. Walton, Journal of Chromatographic Science **40**, 147 (2002).

[104] S. W. Sharpe, T. J. Johnson, R. L. Sams, P. M. Chu, and G. C. Rhoderick, Applied Spectroscopy **58**, 1452 (2004).

[105] "List of Controlled Substances, U.S. Department of Justice, Drug Enforcement Administration," http://www.deadiversion.usdoj.gov/schedules/orangebook/c_cs_alpha.pdf, accessed 1.11.2013.